






# Crystal and solution structure of NDRG1, a membrane-binding protein linked to myelination and tumour suppression

Venla Mustonen<sup>1</sup> , Gopinath Muruganandam<sup>2,3</sup> , Remy Loris<sup>2,3</sup> , Petri Kursula<sup>1,4</sup>  and Salla Ruskamo<sup>1</sup> 

- 1 Faculty of Biochemistry and Molecular Medicine & Biocenter Oulu, University of Oulu, Finland
- 2 VIB-VUB Center for Structural Biology, Vlaams Instituut voor Biotechnologie, Brussels, Belgium
- 3 Structural Biology Brussels, Department of Bioengineering Sciences, Vrije Universiteit Brussel, Belgium
- 4 Department of Biomedicine, University of Bergen, Norway

## Keywords

Charcot-Marie-Tooth disease; crystal structure; myelin; small-angle X-ray scattering; tumour suppressor gene

## Correspondence

S. Ruskamo, Faculty of Biochemistry and Molecular Medicine & Biocenter Oulu, P.O. Box 5400, 90014 University of Oulu, Finland  
 Tel: +358503279168  
 E-mail [salla.ruskamo@oulu.fi](mailto:salla.ruskamo@oulu.fi)

(Received 27 August 2020, revised 27 October 2020, accepted 7 December 2020)

doi:10.1111/febs.15660

N-myc downstream-regulated gene 1 (NDRG1) is a tumour suppressor involved in vesicular trafficking and stress response. NDRG1 participates in peripheral nerve myelination, and mutations in the *NDRG1* gene lead to Charcot-Marie-Tooth neuropathy. The 43-kDa NDRG1 is considered as an inactive member of the  $\alpha/\beta$  hydrolase superfamily. In addition to a central  $\alpha/\beta$  hydrolase fold domain, NDRG1 consists of a short N terminus and a C-terminal region with three 10-residue repeats. We determined the crystal structure of the  $\alpha/\beta$  hydrolase domain of human NDRG1 and characterised the structure and dynamics of full-length NDRG1. The structure of the  $\alpha/\beta$  hydrolase domain resembles the canonical  $\alpha/\beta$  hydrolase fold with a central  $\beta$  sheet surrounded by  $\alpha$  helices. Small-angle X-ray scattering and CD spectroscopy indicated a variable conformation for the N- and C-terminal regions. NDRG1 binds to various types of lipid vesicles, and the conformation of the C-terminal region is modulated upon lipid interaction. Intriguingly, NDRG1 interacts with metal ions, such as nickel, but is prone to aggregation in their presence. Our results uncover the structural and dynamic features of NDRG1, as well as elucidate its interactions with metals and lipids, and encourage studies to identify a putative hydrolase activity of NDRG1.

## Databases

The coordinates and structure factors for the crystal structure of human NDRG1 were deposited to PDB (PDB ID: [6ZMM](https://www.rcsb.org/entry/6ZMM)).

## Abbreviations

AKT, protein kinase B; CMT, Charcot-Marie-Tooth disease; CNS, central nervous system; DMPC, 1,2-dimyristoyl-sn-glycero-3-phosphocholine; DMPG, 1,2-dimyristoyl-sn-glycero-3-phosphoglycerol; DSF, differential scanning fluorimetry; EOM, ensemble optimisation method; HIF-1, hypoxia-inducible factor 1; IP<sub>3</sub>R, inositol 1,4,5-trisphosphate receptor; ITC, isothermal titration calorimetry;  $K_d$ , binding affinity; MALS, multiangle light scattering; mTOR, mammalian target of rapamycin; NDRG1, N-myc downstream-regulated gene 1; PcpA, 2,6-dichloro-p-hydroquinone 1,2-dioxygenase; PI3K, phosphatidylinositol-3-kinase; PI4P, phosphatidylinositol 4-phosphate; PIP, phosphatidylinositol phosphate; PNS, peripheral nervous system; POPC, 1-palmitoyl-2-oleoyl-sn-glycero-3-phosphocholine; SAXS, small-angle X-ray scattering; SEC, size-exclusion chromatography; SGK1, serum and glucocorticoid-regulated kinase 1; SRCD, synchrotron radiation circular dichroism; TEV, tobacco etch virus;  $T_m$ , melting temperature.

## Introduction

The myelin sheath plays a crucial role in increasing the speed of action potentials along neuronal axons in the vertebrate nervous system. Myelin is produced by oligodendrocytes in the central nervous system (CNS) and Schwann cells in the peripheral nervous system (PNS). One of the major characteristics distinguishing myelin from other biological membranes is its high lipid-to-protein ratio: isolated myelin contains at least 70% lipid [1]. The importance of the insulative nature of myelin is highlighted by severe neurological defects caused by myelin loss (demyelination) as a consequence of disease, such as multiple sclerosis, Guillain-Barré syndrome or Charcot-Marie-Tooth disease (CMT).

Charcot-Marie-Tooth disease is the most common hereditary demyelinating neuropathy affecting peripheral nerves, and it can be divided into subtypes based on electrodiagnostic findings and inheritance patterns [2,3]. Several homozygous mutations in *N-myc downstream-regulated gene 1* (*NDRG1*) cause CMT type 4D, which was first identified in the Gypsy community of Lom in Bulgaria [4] and later described in several other European countries [5,6] as well as in China [7,8]. Neuropathological findings in CMT4D point towards Schwann cell dysfunction indicated by demyelination/remyelination and hypomyelination, onion bulb formation and accumulation of pleomorphic material in the adaxonal Schwann cell cytoplasm [9–12]. Axonal involvement is evident by severe, progressive axonal loss and the presence of curvilinear intra-axonal inclusions [10,12]. The founding mutation R148X also affects CNS myelin [13,14]. In addition to humans, a neuropathy with similar symptoms caused by mutations in *NDRG1* has been observed in certain dog breeds, such as Greyhounds [15] and Alaskan Malamutes [16].

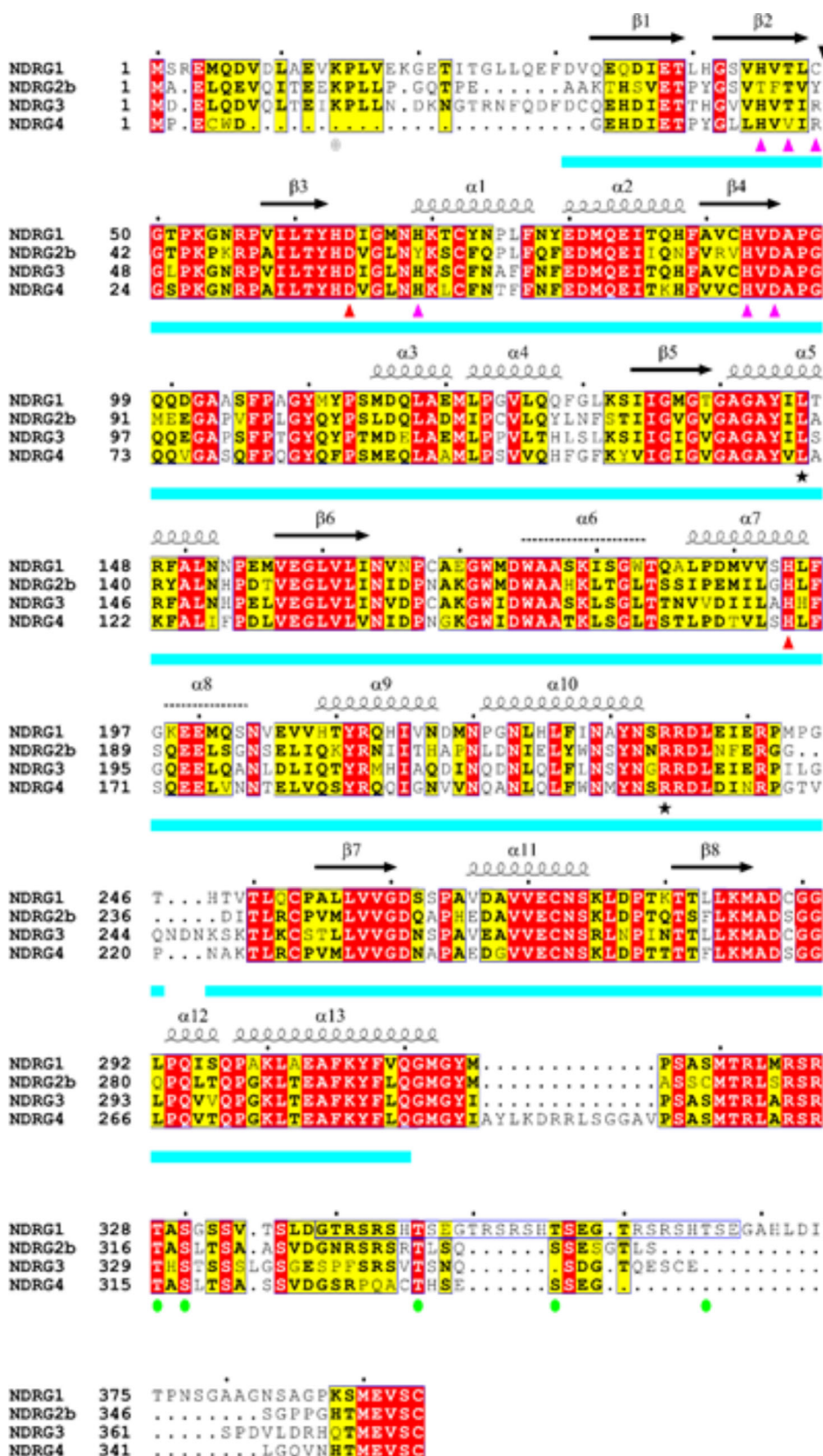
Neuropathological findings suggest that *NDRG1* plays a role in the formation and maintenance of the myelin sheaths in peripheral nerves [17]. In vertebrates, *NDRG1* is largely expressed in oligodendrocytes and Schwann cells [18–21]. In the PNS, *NDRG1* is a target

of the phosphatidylinositol-3-kinase (PI3K)/protein kinase B (AKT)/mammalian target of rapamycin (mTOR) pathway, being phosphorylated in the C terminus by AKT1 in developing nerves [20] and predominantly by serum and glucocorticoid-regulated kinase 1 (SGK1) in adults [20,22]. In murine and canine tissues, phosphorylated *NDRG1* is exclusively localised in the abaxonal cytoplasm of the myelinating Schwann cells, while total *NDRG1* is present throughout the cytoplasm [20,21].

The human *NDRG1* (also known as *CAP43*, *DRG1*, *NDRI*, *PROXY1*, *RIT42*, *RTP* and *TDD5*) is mapped to chromosome 8q24.22 and codes for a 43-kDa protein [4,23]. *NDRG1* forms, together with *NDRG2*, *NDRG3* and *NDRG4*, a protein family, which shares 53–65% sequence identity, the highest identity laying in the area of an  $\alpha/\beta$  hydrolase motif (Fig. 1) [24]. However, *NDRG* proteins seem to lack catalytic activity [25,26], although the  $\alpha/\beta$  hydrolase domain of *NDRG1* was recently suggested to bind fatty acids [27]. Crystal structures of the  $\alpha/\beta$  hydrolase domain of human *NDRG2* isoform 2 (residues 23–304) [26] and human *NDRG3* (residues 29–320) [28] show the absence of a canonical catalytic triad and blockage of a possible substrate-binding cavity by helices  $\alpha 7$  and  $\alpha 10$ . Phylogenetically, *NDRG1* and *NDRG3* belong to one subfamily, while *NDRG2* and *NDRG4* belong to another [24]. *NDRG1* contains three tandem repeats of 10 amino acids (GTRSRSHSTSE) in its C terminus [23], which are absent in the other family members (Fig. 1). *NDRG1* has high evolutionary conservation from plants to humans [29], which suggests an important biological role (Fig. 2). The other *NDRG* family members have not been linked to demyelinating neuropathies [30], although all human CMT4D-related mutations are located in the  $\alpha/\beta$  hydrolase domain of *NDRG1*.

The physiological functions of *NDRG1* have remained ambiguous. In humans, *NDRG1* mRNA is found in most organ systems, and the protein is mainly localised in the cytoplasm; however, the protein can also be found in the nucleus, mitochondria or membranes, depending on the tissue type [18]. In

**Fig. 1.** Sequence alignment of human *NDRG* isoforms. The secondary structure of *NDRG1* is shown above the sequence alignment (predicted helices missing from the crystal structure with dashed lines), and the  $\alpha/\beta$  hydrolase fold of *NDRG1* is marked with a cyan stroke under the alignment. Identical and similar residues are highlighted in red and yellow, respectively. Potential catalytic residues of *NDRG1* are marked with red triangles, and putative metal-binding residues with pink triangles. SGK1-dependent phosphorylation sites, the SUMOylation site and a predicted site for proteolytic cleavage are marked with green circles, a grey circle and a black triangle, respectively. Amino acid substitutions causing CMT4D are marked with black asterisks, and the open blue box indicates the triple decapeptide repeat of *NDRG1*. Sequences were aligned with T-Coffee [97] and visualised using ESPrnt [98]. UniProtKB accession numbers were as follows: *NDRG1* (Q92597-1), *NDRG2b* (Q9UN36-2), *NDRG3* (Q9UGV2-1), *NDRG4* (Q9ULP0-1).



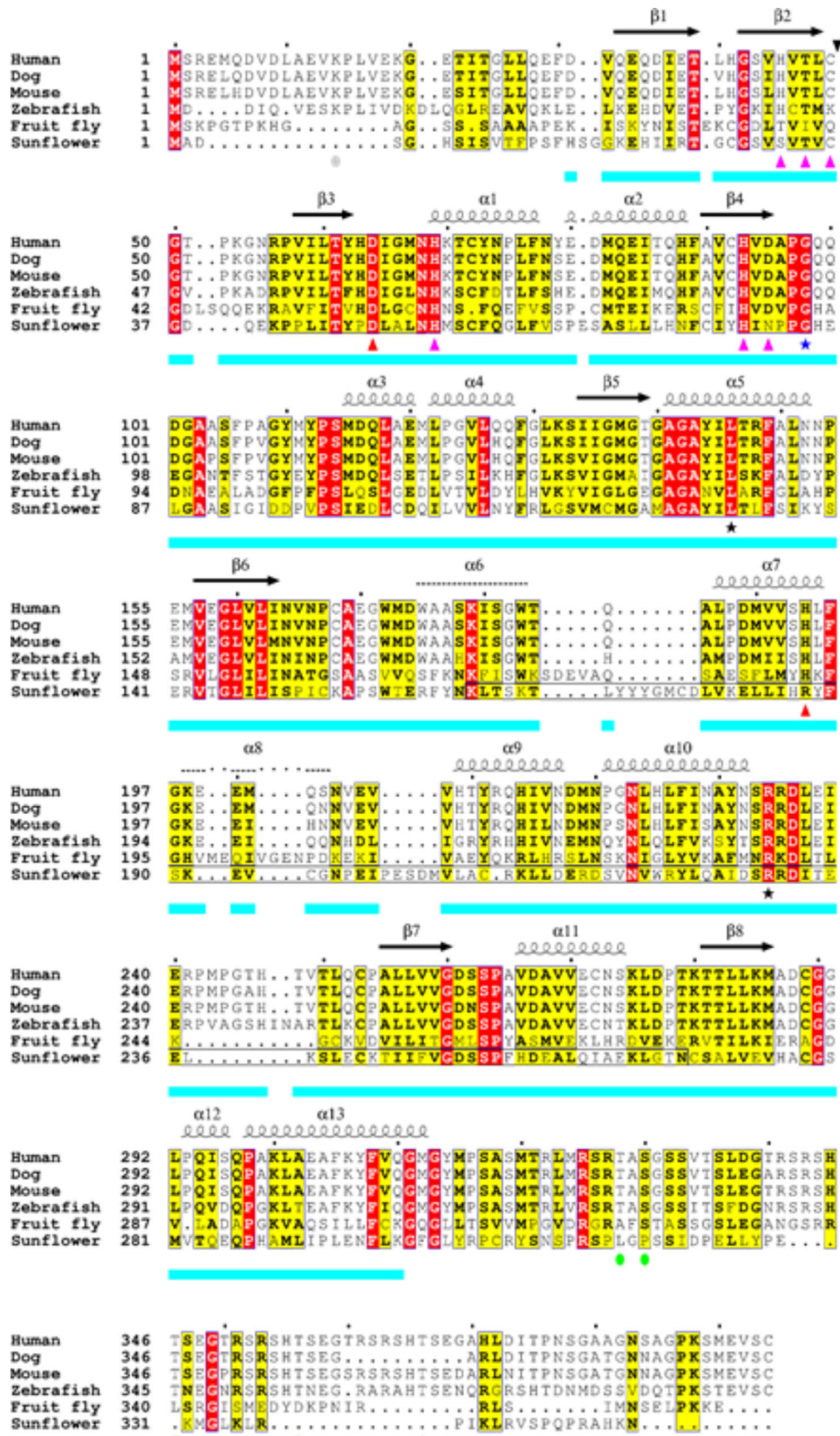


**Fig. 2.** Conservation of NDRG1 between species. Potential catalytic residues (red triangles), putative metal-binding residues (pink triangles), phosphorylation sites (green circles), a SUMOylation site (grey circle) and a predicted proteolytic cleavage site (black triangle) are marked as in Fig. 1. The position of a disease-causing amino acid substitution in dogs (Alaskan Malamute) is marked with a blue asterisk, and the homologous region with vertebrate IP<sub>3</sub>R is marked with an open black box. Sequences were aligned with T-Coffee [97] and visualised using ESPript [98]. UniProtKB accession numbers were as follows: dog NDRG1 (L7V3M2-1), mouse NDRG1 (O62433-1), zebrafish NDRG1 (O6A3P5-1), fruit fly BcDNA : GH02439 (Q9Y164-1) and sunflower pollen-specific protein SF21 (Q23969-1).

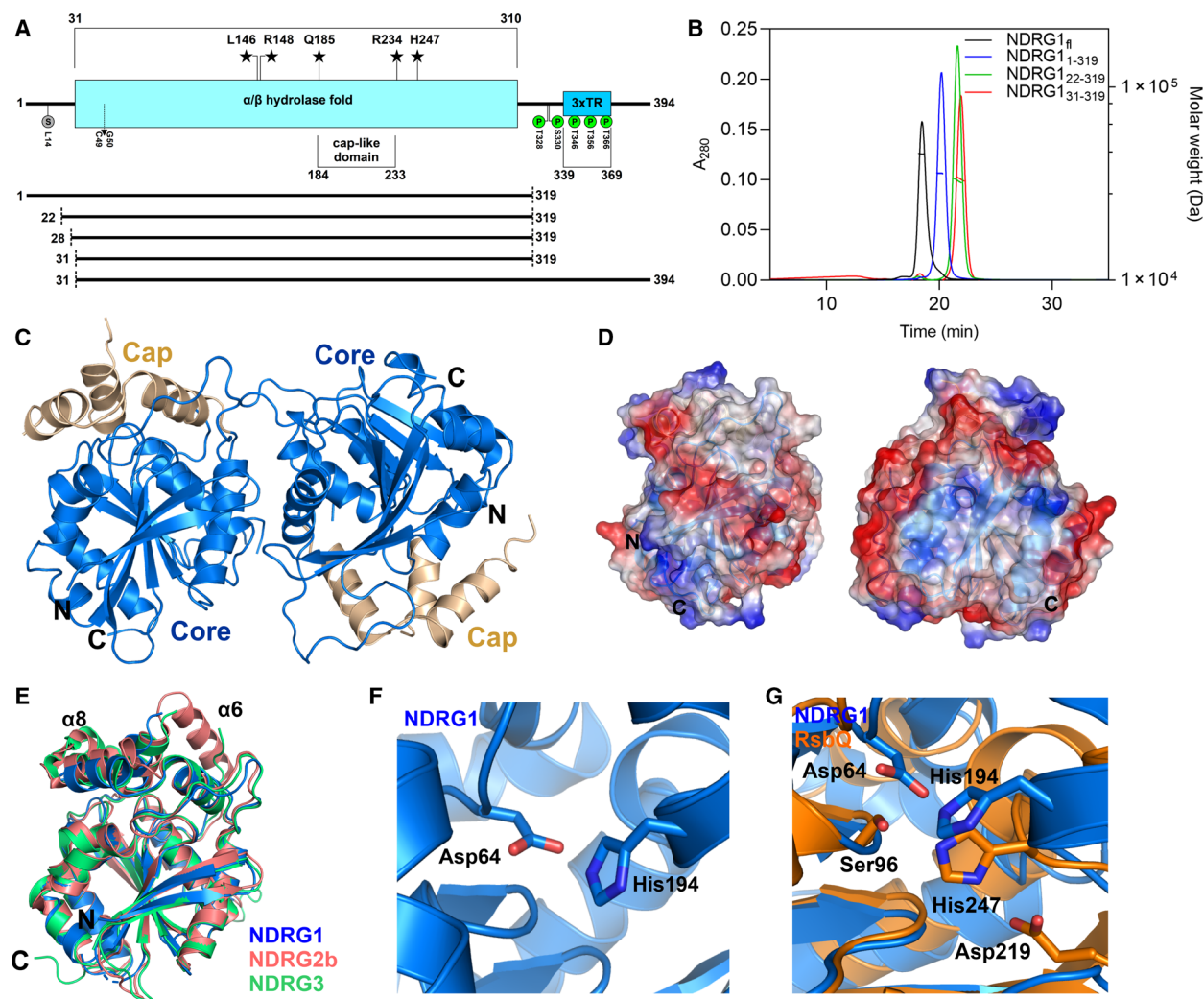


**Fig. 3.** NDRG1 contains a central globular  $\alpha/\beta$  hydrolase fold, an N-terminal 30-residue region and a C-terminal region containing three 10-residue repeats. (A) Schematic view of NDRG1. The  $\alpha/\beta$  hydrolase fold, C-terminal repeat, phosphorylation (P), SUMOylation (S) and predicted proteolytic cleavage (arrow between C49 and G50) sites as well as residues mutated in CMT4D (asterisk) have been marked. The constructs used in this study have been illustrated below. (B) SEC-MALS curves of NDRG1<sub>fl</sub> (black), NDRG1<sub>1-319</sub> (blue), NDRG1<sub>22-319</sub> (green) and NDRG1<sub>31-319</sub> (red). (C) An asymmetric unit contains two NDRG1 molecules; the cap region is marked with beige and the  $\alpha/\beta$  hydrolase fold in blue. Panels C–G were prepared using PyMOL (<https://pymol.org/2/>). (D) Transparent electrostatic surface shown with two views. (E) Superimposition of NDRG1 (blue), NDRG2b (brown) and NDRG3 (green)  $\alpha/\beta$  hydrolase domains indicates minor differences in overall structure. (F) The canonical catalytic site is not present in NDRG1, but potential catalytic amino acids (Asp64 and His194) are located in a nearly equivalent position in the structure. (G) The catalytic site of *Bacillus subtilis* stress-response regulator, RsbQ (orange), superimposed with NDRG1 (blue).

addition to phosphorylation, the N terminus of NDRG1 can be post-translationally modified by proteolytic cleavage [31] and SUMOylation [32] (Fig. 3A). The expression of *NDRG1* can be altered by the proto-oncogenes MYCN and MYC [33,34], p53 and DNA damage [35], PTEN [36], androgens [37], DNA methylation and histone acetylation [38] as well as multiple compounds, such as cysteine, tunicamycin, 2-mercaptoethanol [23] and retinoic acid [39]. In consequence, NDRG1 functions at least in growth arrest [35], cell differentiation [40], p53-mediated apoptosis [41] and centrosome homeostasis [42,43]. NDRG1 is a metastasis suppressor in prostate, breast and colon cancers [44–46].

Hypoxia-inducible factor 1 (HIF-1) plays an important role in cellular responses to hypoxia, including regulation of genes involved in glycolysis, angiogenesis and apoptosis. Nickel, cobalt and iron chelators mimic hypoxia and can induce the expression of *NDRG1* by inducing and stabilising HIF-1 [47–50]. Nickel and cobalt can substitute Fe<sup>2+</sup> in enzymes acting in HIF-1 expression or stabilisation pathways, and iron chelators can prevent the binding of oxygen to haeme groups or degradation of HIF-1 $\alpha$  and HIF-2 $\alpha$  [49,51,52]. Interestingly, NDRG1 might interact with metals directly: a 30-amino acid peptide containing the C-terminal repeats of NDRG1 (TRSRSHSTSE)<sub>3</sub> binds nickel [53,54], copper [55], zinc [56], manganese and cobalt [57].

From a PNS perspective, the most important role of NDRG1 is in cellular trafficking: it interacts with apolipoproteins [58] and cardiolipin [59], regulates LDL receptor trafficking [60] and recycling of E-cadherin [59] and is involved in vesicle transport [61]. NDRG1 recruits on recycling endosomes in the Golgi complex by binding to phosphatidylinositol 4-phosphate (PI4P) and interacts with membrane-bound RAB4a [59]. In addition, NDRG1 interacts with Rab acceptor 1, which is required for lipid transport and vesicle formation from the Golgi complex [62]. In breast cancer cells, NDRG1 regulates neutral lipid metabolism [27], and in cells infected by hepatitis C virus, NDRG1 regulates lipid droplet biogenesis [63]. In prostate cancer cells, NDRG1

interacts with the cell adhesion molecules E-cadherin and  $\beta$ -catenin [64].

Despite extensive research on its physiological function, the structure and biochemical properties of NDRG1 have remained uncharacterised. Thus, we determined the crystal structure of the human NDRG1  $\alpha/\beta$  hydrolase domain and obtained information about the structure and conformational dynamics of full-length NDRG1 using small-angle X-ray scattering (SAXS) and synchrotron radiation circular dichroism (SRCD). Additionally, we used a combined approach of CD, lipid cosedimentation, nanodifferential scanning fluorimetry (nano-DSF) and isothermal titration calorimetry (ITC) to study lipid and metal binding by NDRG1 to better understand its role in lipid transport, vesicular trafficking and stress response. NDRG1 interacts with various types of lipid membranes, and the conformation of the C-terminal region is modulated upon these interactions.

## Results

### NDRG1 is monomeric in solution

No experimental studies on the structural or biochemical characteristics of NDRG1 have been published. Based on secondary structure predictions [65,66], NDRG1 is composed of a short N-terminal region (residues 1–30), a central  $\alpha/\beta$  hydrolase domain including a cap region (residues 31–310) and a flexible C-terminal region consisting of three 10-amino acid (GTRSRSHSTSE) tandem repeats (residues 339–368; Fig. 3A) not found in other NDRG family members (Fig. 1).

To characterise NDRG1, we expressed and purified full-length (fl) human NDRG1 (NDRG1<sub>fl</sub>) as well as truncated forms containing residues 1–319 (NDRG1<sub>1–319</sub>), 22–319 (NDRG1<sub>22–319</sub>), 28–319 (NDRG1<sub>28–319</sub>), 31–319 (NDRG1<sub>31–319</sub>) and 31–394 (NDRG1<sub>31–394</sub>) (Fig. 3A). Most NDRG1 constructs eluted as single peaks in size-exclusion chromatography (SEC), while a minor peak corresponding to a dimer was observed for NDRG1<sub>22–319</sub> and NDRG1<sub>28–319</sub>. NDRG1<sub>31–394</sub> was unstable and degraded during purification. We

**Table 1.** SEC-MALS and SAXS parameters.

Constructs	Calc. MW (kDa)	SEC-MALS MW (kDa)	$R_g$ (Å)	$D_{max}$ (GNOM) (Å)	$D_{max}$ (EOM) (Å)	Porod V (Å <sup>3</sup> )
NDRG1 <sub>fl</sub>	42.8	45.1	28.85 ± 0.08	103	99	79 684
NDRG1 <sub>1–319</sub>	35.0	35.7	23.23 ± 0.07	70	76	59 576
NDRG1 <sub>22–319</sub>	32.5	32.9	19.64 ± 0.03	57.5	n.d.	54 045
NDRG1 <sub>28–319</sub>	32.1	n.d.	19.38 ± 0.03	56.5	n.d.	51 292
NDRG1 <sub>31–319</sub>	31.7	33.4	20.41 ± 0.02	61	n.d.	54 274

**Table 2.** Melting temperatures (°C) for NDRG1 constructs ± various ions, red text indicating increase of ≥ 0.5 °C and blue text indicating decrease of ≥ 0.5 °C.

Constructs	No additive	Mg <sup>2+</sup>	Fe <sup>2+</sup>	Fe <sup>3+</sup>	Co <sup>2+</sup>	Ni <sup>2+</sup>
NDRG1 <sub>fl</sub>	56.5	57.2	56.5	56.6	52.1	48.5
NDRG1 <sub>1–319</sub>	60.0	60.0	59.9	60.1	53.0	46.0
NDRG1 <sub>28–319</sub>	60.5	60.6	60.5	60.5	54.9	46.5
NDRG1 <sub>22–319</sub>	60.0	n.d.	n.d.	n.d.	n.d.	n.d.
NDRG1 <sub>31–319</sub>	58.8	n.d.	n.d.	n.d.	n.d.	n.d.

**Table 3.** Crystallographic data collection and refinement statistics. Statistics for the highest resolution shell are shown in parentheses.

Human NDRG1 (PDB: 6ZMM)	
Wavelength (Å)	0.9762
Resolution range (Å)	47.11–2.963 (3.069–2.963)
Space group	P 4 <sub>3</sub> 2 <sub>1</sub> 2
Unit cell <i>a</i> , <i>b</i> , <i>c</i> (Å)	108.57, 108.57, 119.33
Total reflections	64 600 (25 100)
Unique reflections	14 800 (1405)
Multiplicity	4.26 (4.39)
Completeness (%)	95.66 (93.04)
Mean <i>I</i> /σ( <i>I</i> )	4.33 (1.42)
Wilson <i>B</i> -factor (Å <sup>2</sup> )	63.7
<i>R</i> <sub>meas</sub> (%)	31.1 (125.6)
CC <sub>1/2</sub> (%)	98.5 (75.5)
<i>R</i> <sub>work</sub>	0.2688 (0.4173)
<i>R</i> <sub>free</sub>	0.2948 (0.5360)
RMSD bonds (Å)	0.002
RMSD bond angles (°)	0.58
Ramachandran favoured (%)	95.24
Ramachandran allowed (%)	4.35
Ramachandran outliers (%)	0.41
Rotamer outliers (%)	0.47
Clashscore	4.97
Average <i>B</i> -factor (Å <sup>2</sup> )	65.4

determined the molecular weight of purified NDRG1 using multiangle light scattering (MALS) (Fig. 3B, Table 1), and the observations fitted well to theoretical monomeric molecular weights.

Nano-DSF is a label-free technique for measuring protein stability utilising intrinsic Trp fluorescence of proteins. We used nano-DSF to study the thermal stability of NDRG1. The melting temperature (*T*<sub>m</sub>) of the constructs varied from 56.5 to 60.5 °C (Table 2). NDRG1 stability increased upon C-terminal truncation, while N-terminal truncation did not have a strong effect.

### Crystal structure of the central core domain

Despite comprehensive research on the cellular functions and tumour suppressing characteristics of

NDRG1, no structural characterisation has been done. We determined the crystal structure of the folded core domain of human NDRG1 (residues 31–319) at 2.96-Å resolution (Fig. 3C, Table 3). The asymmetric unit in the crystal contains two NDRG1 molecules (Fig. 3C). The core of NDRG1 is composed of a canonical α/β hydrolase fold with a central eight-stranded β sheet surrounded by α helices and a cap domain. The cap domain is formed by three helices as well as disordered regions, and it covers the top of the α/β hydrolase fold (Fig. 3C). We could not detect electron density for residues 170–184 (putative α6 helix) and 197–201 (putative α8 helix) in either of the NDRG1 chains. These residues are located in the cap domain, and the absence of electron density hints at flexibility of these parts in the NDRG1 structure. The electrostatic surface reveals a ring-shaped negative zone perpendicular to the central β sheet on the surface of NDRG1 (Fig. 3D).

The crystal structures of human NDRG2b and NDRG3 have been determined [26,28]. The sequence identity of the core domain of NDRG1 to NDRG3 and NDRG2b is 73% and 59%, respectively. The overall fold of the α/β hydrolase and cap domains of NDRG1 is similar to NDRG3 and NDRG2b, with RMS deviations of 1.0 and 1.5 Å, respectively (Fig. 3E). In the crystal structure of NDRG2b, all helices of the cap domain are visible, whereas in the NDRG3 structure, the α6 helix is missing. The NDRG1 cap domain resembles more the cap domain of NDRG3 than NDRG2b.

NDRG1 belongs to the α/β hydrolase superfamily, but based on sequence alignments, it lacks the canonical α/β hydrolase catalytic triad [25]. However, a nearly equivalent site in NDRG1 contains aspartate (Asp64) and histidine (His194) residues, located at the end of strand β3 and in the beginning of helix α7, respectively (Fig. 3F–G). Aspartate and histidine are commonly found in catalytic triads of α/β hydrolases. Unfortunately, the electron density for the predicted α6 helix, located on one side of this potential catalytic site, was not clear enough to allow building the structure.

The interface between the two molecules in the asymmetric unit was analysed using PISA [67]. The buried area was ~ 890 Å<sup>2</sup>, and the interactions between the molecules included four hydrogen bonds and two salt bridges. The complex formation significance score was 0.0, indicating that the interaction occurs due to crystal packing and does not exist in solution.

### Structure and flexibility of full-length NDRG1

To elucidate the structural properties of different regions of NDRG1, we performed SRCD

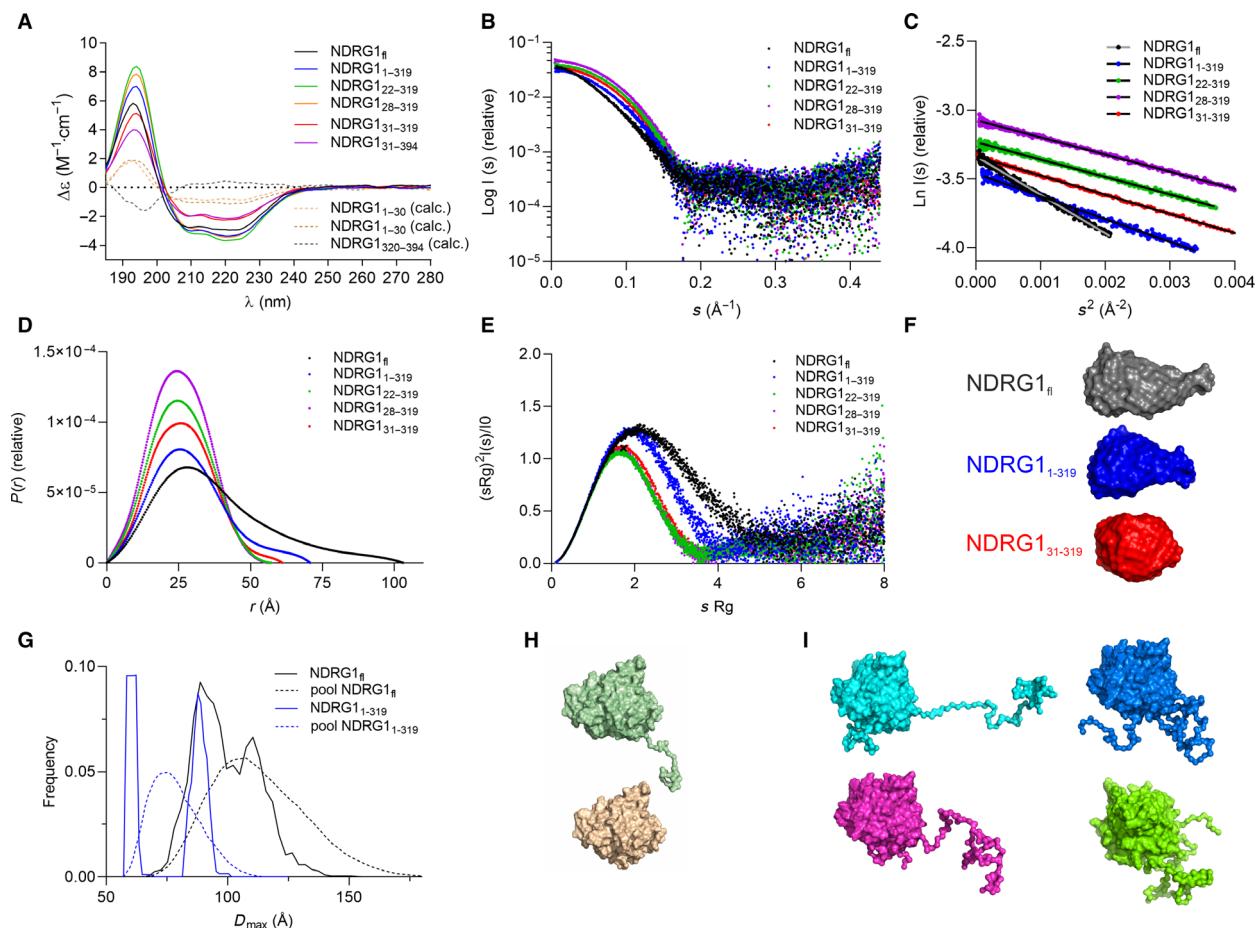


**Fig. 4.** NDRG1 has partially folded N-terminal region, a central globular core domain and disordered C terminus. (A) SRCD spectra for NDRG1 constructs and calculated spectra of the N and C terminus. (B) Scattering patterns for NDRG1 fragments: NDRG1<sub>fl</sub> (black), NDRG1<sub>1-319</sub> (blue), NDRG1<sub>22-319</sub> (green), NDRG1<sub>28-319</sub> (purple), NDRG1<sub>31-319</sub> (red). (C) Linear Guinier regions of NDRG1 constructs confirm the good quality of SAXS data. (D) Distance distribution functions indicate highly elongated confirmation for NDRG1<sub>fl</sub> (black), while NDRG1<sub>22-319</sub> (green), NDRG1<sub>28-319</sub> (purple) are the most compact NDRG1 constructs. (E) Dimensionless Kratky plot suggests a globular shape of constructs containing residues NDRG1<sub>22-319</sub>, NDRG1<sub>28-319</sub> and NDRG1<sub>31-319</sub> whereas NDRG1<sub>1-319</sub> is slightly less globular and rigid and NDRG1<sub>fl</sub> the most flexible. The black cross indicates the theoretical peak position for a rigid globular protein. (F) *Ab initio* models for NDRG1<sub>fl</sub> (grey), NDRG1<sub>1-319</sub> (blue) and NDRG1<sub>31-319</sub> (red). Panels F, H and I were prepared using PYMOL. (G)  $D_{\max}$  distributions from EOM analysis for NDRG1<sub>fl</sub> and NDRG1<sub>1-319</sub> indicate flexible but more compact than random coil peptide for both N- and C-terminal regions; solid lines represent the ensembles for NDRG1<sub>fl</sub> (black) and NDRG1<sub>1-319</sub> (blue) and dashed lines theoretical distribution for random coils. EOM conformations suggest N terminus may fold on the side of the core domain observed in one of the conformations of NDRG1<sub>1-319</sub> (H). EOM suggests rather flexible and disordered nature of the C terminus observed in the pool of conformations of NDRG1<sub>fl</sub> (I).

spectroscopy. All constructs gave SRCD spectra typical for  $\alpha$ -helical proteins, with a maximum close to 194 nm and minima at 208 and 222 nm (Fig. 4A). In the spectra of NDRG1<sub>31-319</sub> and NDRG1<sub>31-394</sub>, these features were slightly weaker, indicating a reduced secondary structure content. In contrast, the fragments lacking the C-terminal region showed more pronounced spectral features, pointing towards a disordered nature of the C-terminal region (Fig. 4A). The deconvolution of the SRCD spectra of NDRG1<sub>fl</sub>, NDRG1<sub>1-319</sub> and NDRG1<sub>31-319</sub> predicted an  $\alpha$ -helical

content of 28.9%, 30.9% and 29.1%, respectively, whereas  $\beta$  sheets were predicted to cover 16.3%, 13.1% and 16.2% of the fragments. The calculated spectra for residues 1–30 indicate partial folding of the N-terminal region, while the calculated spectrum for the C terminus is typical for a random coil with a clear peak minimum at 198 nm.

Small-angle X-ray scattering is powerful technique to study proteins with flexible regions, such as NDRG1. We collected SEC-SAXS data for NDRG1 constructs (Fig. 4B). All constructs behaved well in



SAXS and gave linear Guinier regions (Fig. 4C). The scattering patterns (Fig. 4B),  $R_g$  and  $D_{max}$  of NDRG1 core fragments illustrate a globular shape ( $D_{max}$  57.5, 56.5 and 61.0 Å for NDRG1<sub>22–319</sub>, NDRG1<sub>28–319</sub> and NDRG1<sub>31–319</sub>, respectively), while NDRG1<sub>1–319</sub> adopts slightly more extended conformation ( $D_{max}$  70 Å), and NDRG1<sub>fl</sub> is remarkably more elongated, with a  $D_{max}$  of 103 Å (Table 1). None of the fragments showed signs of a second distinct globular domain in the pair distance distribution (Fig. 4D). Based on the dimensionless Kratky plot, NDRG1<sub>fl</sub> has the highest flexibility, whereas NDRG1<sub>1–319</sub> is more flexible compared to the most globular core fragments (Fig. 4E). Thus, the N- and C-terminal regions are flexible additions to the rigid, globular core domain.

Keeping in mind the flexible nature of the longer NDRG1 variants, we built *ab initio* chain-like models to illustrate the average shape and dimensions of NDRG1 in solution. The core domain is compact and globular, resembling the crystal structure. The envelopes of the NDRG1<sub>1–319</sub> and NDRG1<sub>fl</sub> constructs ( $\chi^2 = 1.0–1.1$ ) have an extension on one side of the globular domain (Fig. 4F).

The ensemble optimisation method (EOM) has been developed for flexible and intrinsically disordered proteins, allowing to generate an ensemble of conformations, which together reproduce the measured SAXS pattern [68]. EOM gives insight into flexibility and partially folded and dynamic regions in proteins. Utilising the crystal structure of the core domain and the scattering profile of NDRG1<sub>1–319</sub>, an ensemble of N-terminal conformations was modelled. EOM resulted in two conformations ( $\chi^2 = 1.1$ ); a compact conformation ( $D_{max}$  60 Å), with the N-terminal region folded on the core domain, comprises ~ 55% of the particles. In the second conformation, the N terminus is more elongated ( $D_{max}$  89 Å), disordered and flexible (Fig. 4G,H).

Similarly, we analysed the conformation ensemble of the NDRG1<sub>fl</sub> in solution. The obtained ensemble of four conformations fit well to the experimental data ( $\chi^2 = 1.0$ ). Within the NDRG1<sub>fl</sub> ensemble, the N-terminal region occasionally folds onto the core domain, while the C terminus is disordered (Fig. 4I). The C-terminal region is apparently less flexible than a random coil peptide, and it can also adopt a compact conformation (Fig. 4I). The above results point towards a dynamic nature of both the N and C termini of NDRG1.

### NDRG1 interacts with nickel and other metal ions

Nano-DSF can be utilised for studying protein stability in the presence of various additives, such as metal

ions or protein ligands. We investigated the effects of metal ions on the thermal stability of NDRG1<sub>fl</sub>, NDRG1<sub>1–319</sub> and NDRG1<sub>28–319</sub>. Fifty micromolar Fe<sup>2+</sup>, Fe<sup>3+</sup>, Mg<sup>2+</sup> did not affect the  $T_m$  of any construct while Co<sup>2+</sup> and Ni<sup>2+</sup> destabilised all variants (Fig. 5A, Table 2). The effect was more pronounced with NDRG1<sub>1–319</sub> and NDRG1<sub>28–319</sub> than with NDRG1<sub>fl</sub>. Zn<sup>2+</sup> caused precipitation of NDRG1<sub>fl</sub> immediately upon addition.

To study the effect of metals on the secondary structure content of NDRG1<sub>fl</sub>, we performed CD spectroscopy. The  $\alpha$ -helical content of NDRG1<sub>fl</sub> increased at low concentrations of Ni<sup>2+</sup> or Fe<sup>2+</sup> (Fig. 5B,C); in the presence of 50  $\mu$ M Ni<sup>2+</sup> and Fe<sup>2+</sup>, the  $\alpha$ -helical content increased from 22% to 25–26%. On the other hand, in the presence of Co<sup>2+</sup> NDRG1 lost 10% of its  $\alpha$ -helical content (Fig. 5D).

NDRG1 expression is induced by nickel and cobalt [69] as well as upon iron chelation [49]. The C-terminal region of NDRG1 has been reported to directly interact with nickel [53,54], copper [55], zinc [56], manganese and cobalt [57]. The nickel-binding capacity of NDRG1<sub>fl</sub>, NDRG1<sub>1–319</sub> and NDRG1<sub>28–319</sub> was investigated by ITC. The binding affinity ( $K_d$ ) of all constructs is in the same range (Fig. 5E,F, Table 4). The stoichiometry was close to 1 and was fixed to 1 for all constructs since the concentrations were too low for accurately refining all parameters. Both truncated constructs showed slightly higher affinity than NDRG1<sub>fl</sub>, indicating involvement of the core domain in nickel binding.

### NDRG1 folds upon lipid vesicle binding

NDRG1 is involved in several cellular lipid-related phenomena, such as vesicle and receptor transport [60,61] and lipid droplet biogenesis [63]. Hence, we investigated the interaction of NDRG1 with lipid membranes using unilamellar vesicles as a model system. In lipid cosedimentation assays, more than half of NDRG1<sub>fl</sub> cosedimented with 1-palmitoyl-2-oleoyl-sn-glycero-3-phosphocholine (POPC) vesicles, while in the absence of lipids, the protein remained in the supernatant. These results indicate the binding of NDRG1<sub>fl</sub> to POPC vesicles (Fig. 6A). Variants lacking the C terminus (NDRG1<sub>1–319</sub>) or containing only the core domain (NDRG1<sub>28–319</sub>) showed less binding to POPC vesicles (Fig. 6A).

The interaction of NDRG1 with 1,2-dimyristoyl-sn-glycero-3-phosphocholine : 1,2-dimyristoyl-sn-glycero-3-phosphoglycerol (DMPC : DMPG) vesicles, in which the membrane surface has a negative charge, was explored. DMPC : DMPG (1 : 1) vesicles pulled

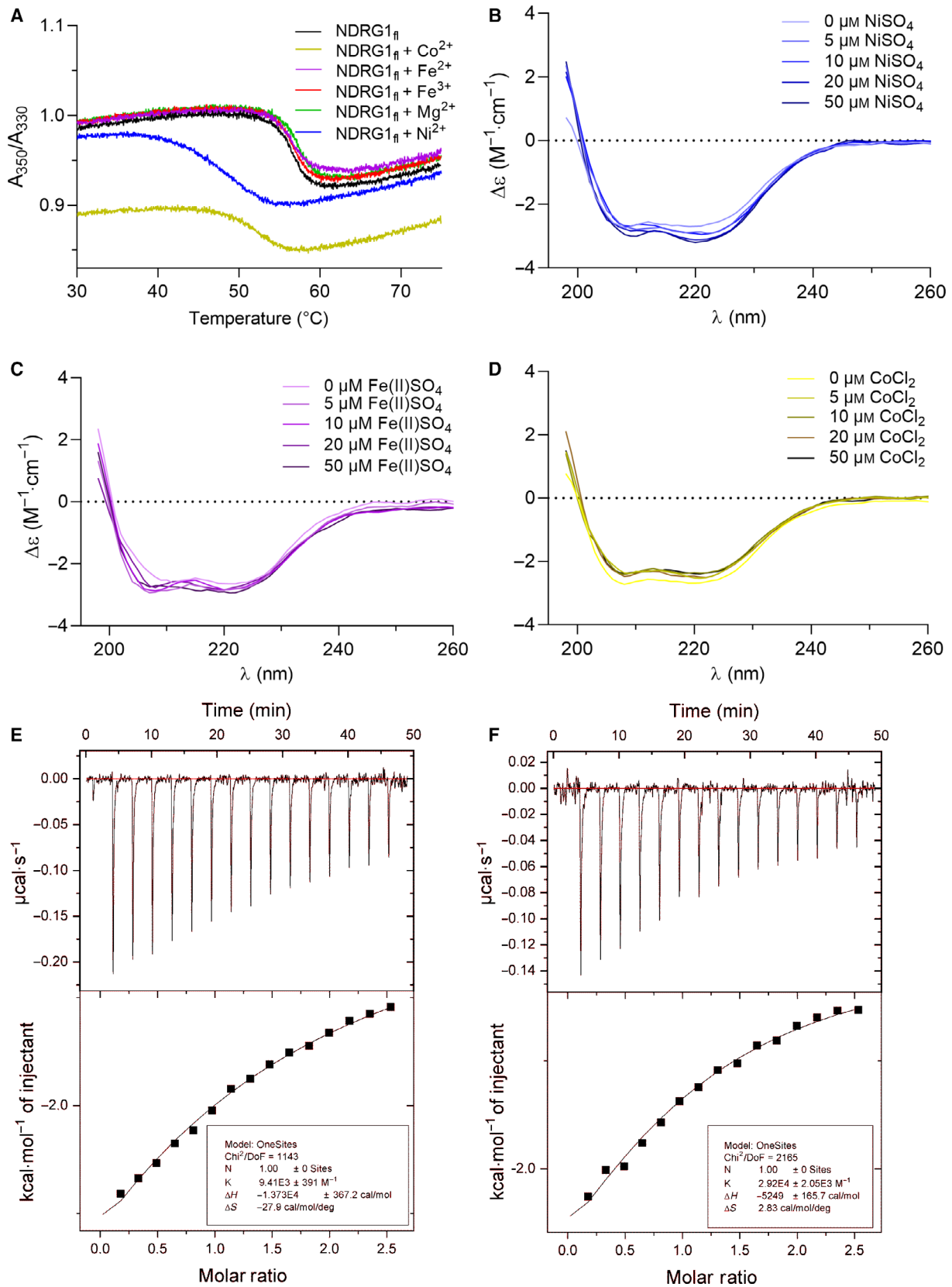


**Fig. 5.** NDRG1 is metal-sensitive and interacts with nickel. (A) DSF curves of NDRG1<sub>fl</sub> alone (black) and in the presence of Co<sup>2+</sup> (yellow), Ni<sup>2+</sup> (blue), Fe<sup>2+</sup> (purple), Fe<sup>3+</sup> (red) and Mg<sup>2+</sup> (green) show major effects of Ni<sup>2+</sup> and Co<sup>2+</sup> on protein stability. The CD spectra for NDRG1<sub>fl</sub> in the presence of 0, 5, 10, 20 and 50  $\mu\text{M}$  NiSO<sub>4</sub> (blue) (B), FeSO<sub>4</sub> (purple) (C) or CoCl<sub>2</sub> (yellow) (D). E ITC titration of NiSO<sub>4</sub> to NDRG1<sub>fl</sub> gives a  $K_d$  of 106  $\mu\text{M}$ , whereas NDRG1<sub>1-319</sub> shows slightly higher affinity towards Ni<sup>2+</sup> (F).

down  $\sim 50\%$  of NDRG1<sub>fl</sub>, while only  $\sim 35\%$  cosedimented with the less negatively charged DMPC : DMPG (9 : 1) vesicles. In contrast, both NDRG1<sub>1-319</sub> and NDRG1<sub>28-319</sub> showed an overall reduced binding affinity towards DMPC : DMPG vesicles (Fig. 6B).

To study whether the conformation of the flexible N- and C-terminal regions was affected by binding to POPC or DMPC : DMPG vesicles, we carried out CD spectroscopy for NDRG1<sub>fl</sub> and NDRG1<sub>1-319</sub> in the presence and absence of vesicles. With POPC, a spectral change was observed with both constructs, but the change was more prominent for NDRG1<sub>fl</sub> (Fig. 6C), indicating that the C-terminal region may enhance POPC binding but is not crucial for the interaction. DMPC : DMPG (1 : 1) induced a clear change in the CD spectrum of NDRG1<sub>fl</sub> (Fig. 6C, left panel), whereas only a minor change was seen for NDRG1<sub>1-319</sub> (Fig. 6C, right panel). DMPC : DMPG (9 : 1) did not induce a conformational change in NDRG1<sub>fl</sub>. Based on these data, the flexible C-terminal region is involved in NDRG1 binding to POPC and DMPC : DMPG (1 : 1) vesicles, and the C terminus adopts a more  $\alpha$ -helical conformation upon binding to vesicles. The conformation of the N terminus, in contrast, does not change in the presence of POPC or DMPC : DMPG vesicles, and this region may not be involved in membrane binding.

NDRG1 participates in phosphatidylinositol phosphate (PIP)-related cellular processes, such as membrane trafficking [59] and cell signalling [70]. NDRG1 was reported to bind to PI4P [59], but no information about direct interactions between NDRG1 and other PIPs exists. We studied the effect of PIPs on NDRG1 membrane binding by incorporating various PIPs,

PIP<sub>2S</sub> and PIP<sub>3</sub> into POPC vesicles and following their effects on lipid cosedimentation of NDRG1. Fifty to sixty percent of NDRG1<sub>fl</sub> was pulled down to the pellet regardless of the type of PIP, and no specificity towards any PIP was observed (Fig. 7A). NDRG1<sub>1-319</sub>, in contrast, showed marginally reduced binding to all PIP-containing vesicles (Fig. 7B), while the central core domain was not affected (Fig. 7C).

CD spectroscopy was utilised to reveal the influence of PIP-containing vesicles on the conformation of NDRG1<sub>fl</sub> and NDRG1<sub>1-319</sub>. PI4P, PI(3,5)P<sub>2</sub>, PI(4,5)P<sub>2</sub> and PI(3,4,5)P<sub>3</sub> gave stronger minima at 208 and 222 nm compared to POPC control vesicles, whereas PI5P and PI(3,4)P<sub>2</sub> reduced the secondary structure content of NDRG1<sub>fl</sub> (Fig. 7D). The CD spectra of NDRG1<sub>1-319</sub> were not affected by PIPs (Fig. 7E).

As NDRG1 interacted with Ni<sup>2+</sup>, we wanted to explore whether lipids and metals compete or cooperate in NDRG1 binding. In addition to Ni<sup>2+</sup>, the effects of Fe<sup>2+</sup>, Zn<sup>2+</sup> and Mg<sup>2+</sup> on POPC binding were investigated. Ni<sup>2+</sup> slightly increased the cosedimentation with POPC vesicles, but none of the ions reduced the POPC binding of NDRG1<sub>fl</sub> (Fig. 7F), demonstrating that the lipid- and metal-binding sites in NDRG1 do not compete with each other.

## Discussion

NDRG1 is involved in several pathological conditions, such as CMT4D [4] and various cancers [36,38,46]. Its function as a tumour suppressor has been widely explored, but the structural and dynamical features of the NDRG1 molecule have remained obscure. In this study, we determined the crystal structure of the  $\alpha/\beta$  hydrolase domain of human NDRG1 and studied the structural and biochemical properties of full-length NDRG1, including interactions with lipids and metal ions.

### $\alpha/\beta$ hydrolase fold of NDRG1

We solved the crystal structure of construct NDRG1<sub>31-319</sub>, comprising the  $\alpha/\beta$  hydrolase domain of NDRG1. NDRG1 has two molecules in the asymmetric unit, whereas the asymmetric unit of NDRG3 contains six molecules, and NDRG3 dimerisation

**Table 4.** Thermodynamic parameters of Ni<sup>2+</sup> binding determined by ITC.

Parameters	NDRG1 <sub>fl</sub>	NDRG1 <sub>1-319</sub>	NDRG1 <sub>28-319</sub>
$K_a \times 10^3$ (M <sup>-1</sup> )	9.41 $\pm$ 0.39	29.2 $\pm$ 2.03	30.6 $\pm$ 2.24
<i>N</i>	1	1	1
$\Delta H$ (kcal·mol <sup>-1</sup> )	1.37 $\pm$ 3.67	-5.25 $\pm$ 0.17	-2.03 $\pm$ 0.65
$\Delta S$ (cal·mol <sup>-1</sup> ·deg <sup>-1</sup> )	27.9	2.83	13.7
$K_d$ ( $\mu\text{M}$ )	106	34.3	32.7

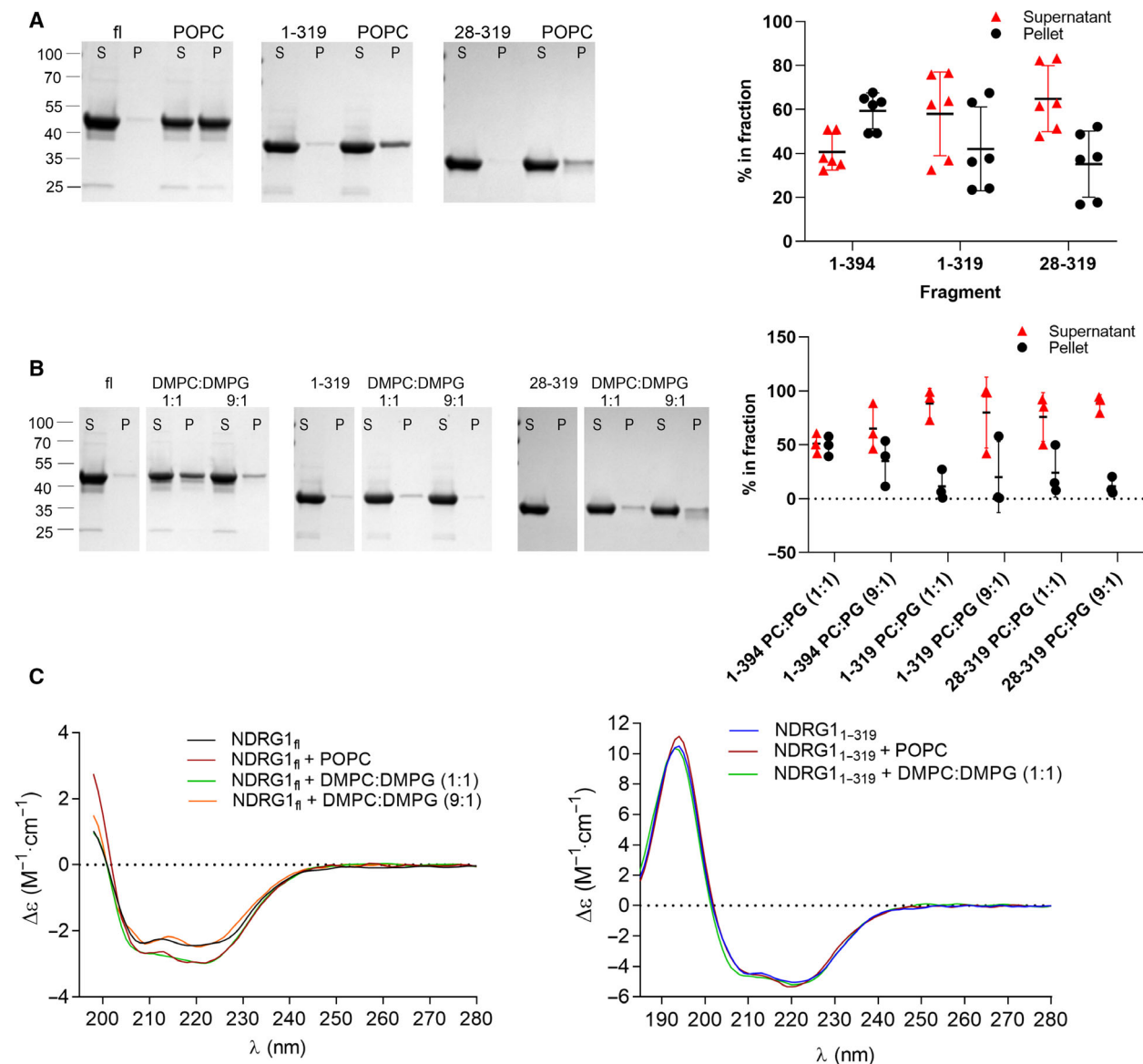


**Fig. 6.** NDRG1 interacts with lipid vesicles. (A) Representative SDS/PAGE analysis of POPC vesicle cosedimentation assay. S, supernatant; P, pellet. Pellet fractions are shown as black circles and supernatant as red triangles, single data points ( $n = 6$ ) as well as the average and SD are shown (right panel). Sixty percent of NDRG1<sub>fl</sub> cosedimented with electrically neutral POPC vesicles whereas  $\sim 40\%$  of NDRG1<sub>1-319</sub> and  $< 40\%$  of NDRG1<sub>28-319</sub> fragment was pelleted. (B) A representative SDS/PAGE analysis of DMPC : DMPG vesicle cosedimentation assay.  $N = 3$  per sample. Fifty percent of NDRG1<sub>fl</sub> was pelleted with negatively charged DMPC : DMPG (1 : 1) vesicles, and the protein pelleted slightly less when less negatively charged DMPC : DMPG (9 : 1) vesicles were used. NDRG1<sub>1-319</sub> and NDRG1<sub>28-319</sub> remained mainly in the supernatant. (C) CD spectra for NDRG1<sub>fl</sub> (black) in the presence of POPC (red), DMPC : DMPG (1 : 1) (green) and (9 : 1) vesicles (orange; left panel) indicate the NDRG1<sub>fl</sub> adopts more secondary structure in the presence of POPC and DMPC : DMPG (1 : 1). The same phenomenon is not observed with DMPC : DMPG (9 : 1) vesicles with NDRG1<sub>1-319</sub> (right panel).

takes place in solution (64). Based on SEC-MALS (Fig. 3B) and structural analyses, NDRG1 is a monomer similarly to NDRG2b [26], illustrating a monomeric biological unit for these proteins.

The NDRG1 crystal structure lacks electron density for helices  $\alpha 6$  and  $\alpha 8$ . Flexible, disordered regions in proteins often play a fundamental role in protein–protein interactions or ligand binding. Such regions may fold and rigidify upon binding to a substrate or an

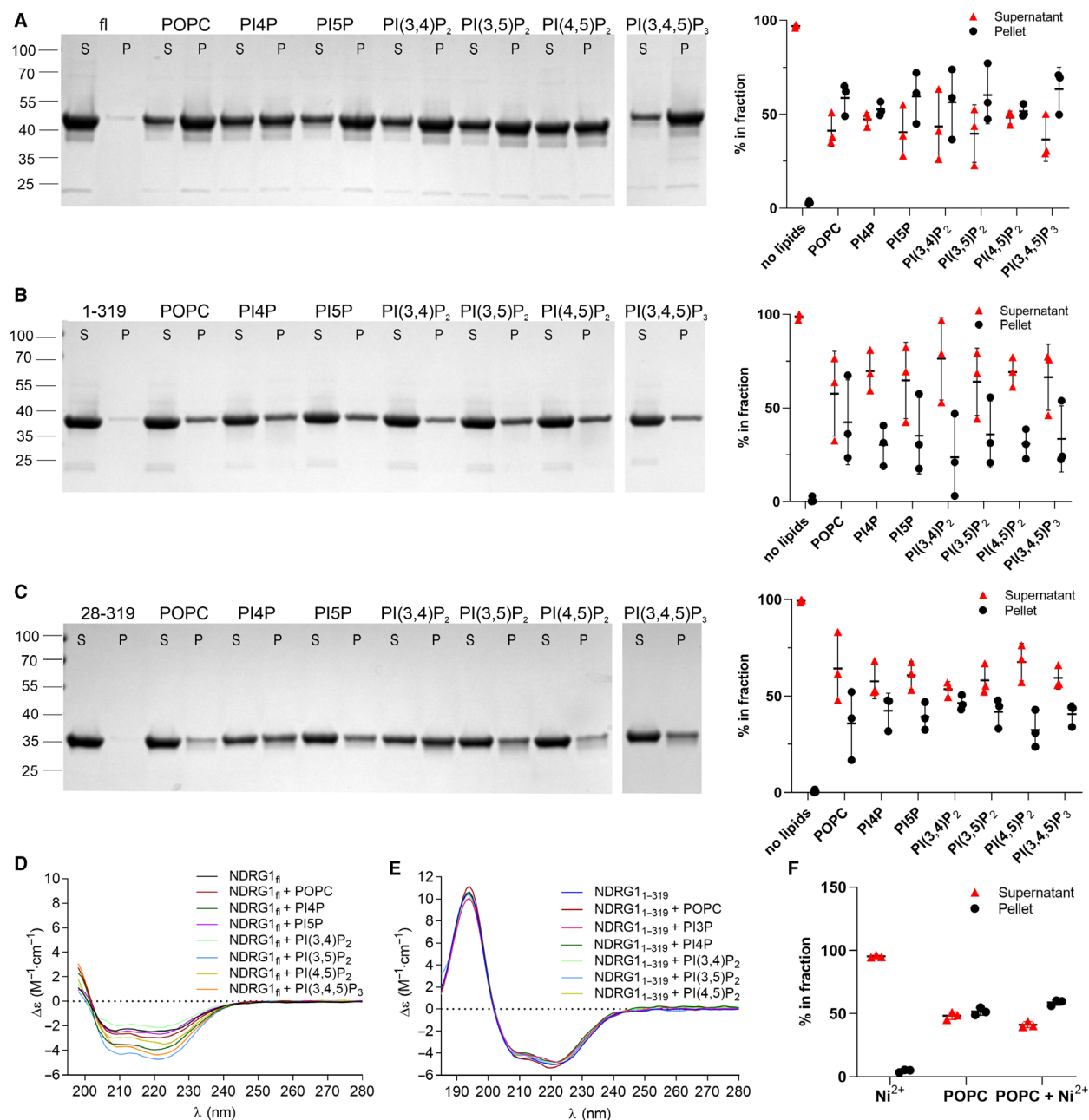


**Fig. 7.** NDRG1 interaction with PIPs and potential competition between lipid vesicles and nickel binding. (A) A representative SDS/PAGE (left panel; S, supernatant; P, pellet) and a graph (right panel) showing the proportions of NDRG1<sub>fi</sub> in the pellet (black circles) and supernatant (red triangles) fractions when various PIPs (10%) were incorporated into POPC vesicles. Individual data points as well as average and SD are marked. PIPs did not remarkably alter the lipid vesicle binding of NDRG1<sub>fi</sub>. (B) The same assay with NDRG1<sub>1-319</sub> showed reduced binding to lipid vesicles containing PIPs. (C) NDRG1<sub>28-319</sub> showed stronger binding to PIP vesicles than NDRG1<sub>1-319</sub>, but still weaker than NDRG1<sub>fi</sub>. (D) CD spectra of NDRG1<sub>fi</sub> in the presence of PIP-POPC lipid vesicles. PI4P, PI(3,5)P<sub>2</sub>, PI(4,5)P<sub>2</sub> and PI(3,4,5)P<sub>3</sub> induced NDRG1<sub>fi</sub> to adopt more  $\alpha$  helical conformation than POPC alone. (E) With NDRG1<sub>1-319</sub>, the same phenomenon was not seen in SRCD measurements. (F) POPC vesicle cosedimentation of NDRG1<sub>fi</sub> in the absence and presence of 50  $\mu$ M NiSO<sub>4</sub>. As a control, the sedimentation of NDRG1<sub>fi</sub> was carried out in the presence of NiSO<sub>4</sub> alone.  $N = 3$  per sample for cosedimentation analyses.

interaction partner. To shed light on whether this happens in the NDRG1 cap domain, further studies will be required with interaction partners or ligands. For NDRG2, the  $\alpha 6$  helix is important for interaction with  $\beta$ -catenin [26]. Helix  $\alpha 6$  is highly conserved among NDRGs (Fig. 1), but structural features are different [28]. How these differences affect  $\beta$ -catenin binding remains unclear.

Based on sequence alignments, NDRG1 has been predicted to be an inactive member of the  $\alpha/\beta$  hydrolase family [25]. However, a region nearby the canonical catalytic site resembles a catalytic triad, having histidine (His194) and aspartate (Asp64) in close proximity (Fig. 3F). These two residues are conserved in all human NDRGs (Fig. 1) as well as in all animal NDRG1s and its homologs (Fig. 2). The third residue of a possible triad is not visible in our structure; the predicted  $\alpha 6$  helix would be located nearby. Cys168, which is located in the beginning of the flexible region and points outwards in our structure, could in theory make the catalytic triad complete. This Cys is found in all vertebrate NDRG1s as well as in human NDRG3, but in neither NDRG2 nor NDRG4 (Figs 1 and 2). The flexible nature of the  $\alpha 6$  helix potentially leaves enough space for a putative substrate; however, in the absence of known substrate we did not perform assays for hydrolase activity. In an earlier study, human NDRG2 did not show detectable hydrolase activity towards *p*-nitrophenyl butyrate [26]. To conclude, the NDRG1 crystal structure raises the possibility that the site formed by His194, Asp64 and Cys168, close to the

canonical active site, could catalyse an as-of-yet unknown enzymatic reaction.

On the other side of the NDRG1  $\alpha/\beta$  hydrolase domain, close to the N terminus, there is a cluster of histidine residues (His45, His69, His93) communed with Thr47, Cys49 and Asp95 (Fig. 8A). Apart from Cys49, these residues are conserved in human NDRG3 and vertebrate NDRG1s (Figs 1 and 2). Similar 3D motifs are found in the active sites of metalloenzymes, in which histidine residues often coordinate a metal ion, such as  $\text{Ni}^{2+}$ ,  $\text{Zn}^{2+}$ ,  $\text{Fe}^{2+}$ ,  $\text{Fe}^{3+}$  or  $\text{Mn}^{2+}$  [71,72]. This histidine-rich site in NDRG1 closely resembles the active site arrangement in 2,6-dichloro-*p*-hydroquinone 1,2-dioxygenase (PcpA), an oxidoreductase from *Sphingobium chlorophenolicum* (Fig. 8B).  $\text{Fe}^{3+}$  is bound to the active site of PcpA and involved in catalysis [71]. We observed effects of several metal ions on NDRG1 stability and conformation and confirmed  $\text{Ni}^{2+}$  binding to the NDRG1 core domain. Nickel competes with essential metals for ligands and binding sites. Nickel induces DNA damage by binding to DNA and nuclear proteins, as well as by catalysing reactive oxygen species production, especially by interfering with iron transport causing hypoxia [73]. *NDRG1* is induced by a rise in free intracellular  $\text{Ca}^{2+}$  following nickel exposure, while, for example, zinc, cobalt, copper, iron(II) and magnesium do not induce its expression [47]. NDRG1 is suggested to act as a nickel chelator through detoxification [53]. In addition, the neurodegenerative disorders Alzheimer's disease and Parkinson's disease are characterised by an

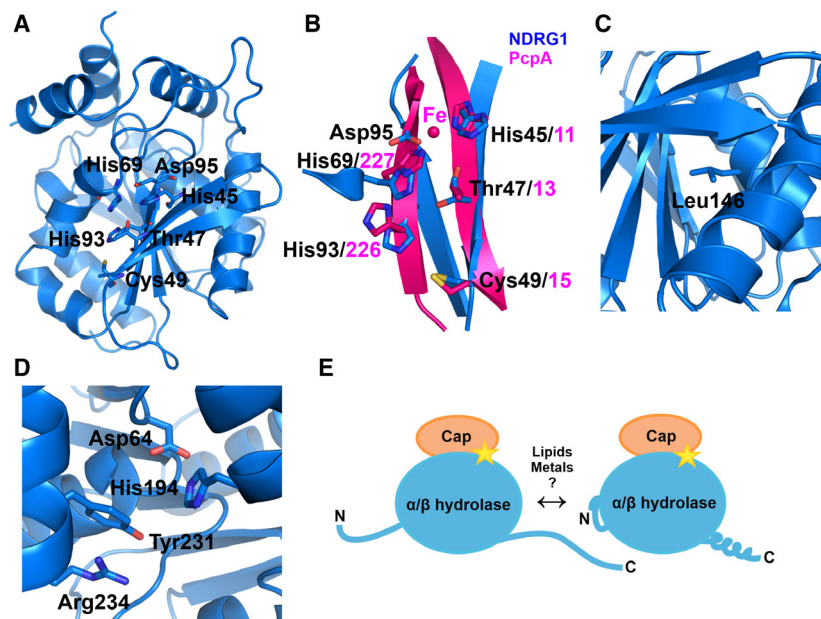


**Fig. 8.** Structural details of NDRG1. (A) The histidine-rich region is located close to the N terminus of the  $\alpha/\beta$  hydrolase fold. Panels A–D were prepared using PYMOL. (B) The histidine-rich region resembles the active site of PcpA oxidoreductase from *Sphingobium chlorophenolicum* (pink) superimposed with NDRG1 (blue). Important residues are shown as sticks and  $\text{Fe}^{3+}$  coordinated by PcpA sidechains as a pink sphere. (C) A point mutation in Leu146 leads to CMT4D. Leu146 is located in the middle of an  $\alpha$  helix in the central part of the  $\alpha/\beta$  hydrolase fold. (D) R234Q mutation has been found in CMT4D. Arg234 is in the close proximity of the canonical active site and forms a  $\pi$ - $\pi$  stacking interaction with Tyr231. (E) A schematic overview of NDRG1 structural features and the conformational changes.

accumulation of metals, such as iron, copper, zinc, manganese and calcium, and by increased levels of oxidative stress, supporting the importance of essential metal homeostasis in the brain [74,75]. NDRG1 interacts with the DNA repair enzyme MGMT [76], while *MGMT* can be epigenetically silenced by nickel [77]. The determination of the binding sites in the NDRG1 core domain, the effects of metal binding on NDRG1 function and putative enzyme activity and the affinity of NDRG1 towards various metals remain to be clarified in further studies.

### The NDRG1 N terminus is dynamic

The N-terminal region is rather conserved between NDRG1 and NDRG3 (Fig. 1). Our structural analysis, based on SRCD and SAXS, shows the N terminus may adopt a compact  $\alpha$ -helical conformation and fold on the side of the  $\alpha/\beta$  hydrolase domain. The N terminus contains several hydrophobic residues, which are unlikely to be exposed. This endorses a model with the N terminus folding onto the  $\alpha/\beta$  hydrolase domain. The fact that we were unable to crystallise NDRG1<sub>1–319</sub> supports the results of the EOM analysis, in which two N-terminal conformations were obtained (Fig. 4H). These conformations could, for example, allow an autoregulatory mechanism of NDRG1 function. Such cases have been observed in phenylalanine hydroxylases, which contain an autoinhibitory N-terminal sequence reaching into the active site. Part of the N-terminal residues are mobile, but the mobility decreases upon the addition of phenylalanine [78]. Similarly, *Candida rugosa* lipase has an N-terminal lid with two conformations: open with the hydrophobic face directed towards the active site and closed with the hydrophobic face buried against the core, covering the active site [79].

In lipid cosedimentation assays, NDRG1<sub>1–319</sub> showed remarkably reduced binding to all lipid vesicles with a negative charge. NDRG1<sub>1–319</sub> had higher affinity towards neutral lipid vesicles, which could allow participation in neutral lipid homeostasis, as observed in studies on NDRG1 in breast cancer cells [27]. Lipid binding had no effect on the folding of the N-terminal region, excluding the possibility that the conformation of the N terminus is directly regulated by the binding to lipid membranes.

### C-terminal region may fold upon interactions and is responsible for binding to various PIPs

Human NDRG1 contains a C-terminal region not found in other NDRGs. This 75-residue region in human NDRG1 contains three 10-residue repeats, but the

number of repeats varies between species (Fig. 1). Each repeat includes a histidine residue, which can coordinate a nickel, copper, zinc, manganese or cobalt ion [53,55–57]. We revealed that the NDRG1 C terminus is dynamic and mainly disordered but may fold upon binding to lipid vesicles or metal ions, such as Ni<sup>2+</sup> or Fe<sup>2+</sup>. Surprisingly, in ITC experiments, NDRG1<sub>fl</sub> had no increased affinity towards Ni<sup>2+</sup> compared with NDRG1<sub>1–319</sub> or NDRG1<sub>28–319</sub>. This supports the hypothesis of an additional metal-binding site in the  $\alpha/\beta$  hydrolase domain of NDRG1.

The C-terminal region is important for NDRG1 membrane interactions. This region is mainly composed of charged residues, and only a few hydrophobic residues exist. The amino acid composition suggests the C terminus is not embedded into a lipid bilayer, but NDRG1 interaction with membranes mainly occurs via lipid head groups. Negatively charged lipids resulted in a conformational change in the C terminus. All PIPs have a negatively charged head group, but interestingly, only some of them induced a conformational change in NDRG1. We could not see clear differences between various PIPs in lipid cosedimentation, but in CD spectroscopy, PI4P, PI(3,5)P<sub>2</sub>, PI(4,5)P<sub>2</sub> and PI(3,4,5)P<sub>3</sub> had a positive effect on folding. Similarly, recent studies on the myelin protein P2 indicated that while headgroup negative charge is important for binding to a membrane surface, the lipid composition has an effect on binding-related conformational changes and possibly function [80]. Previously, using an overlay assay, NDRG1 was reported to bind PI4P but not PI(4,5)P<sub>2</sub> or PI(3,4,5)P<sub>3</sub> [59]. PI4P is an abundant component of *trans*-Golgi membranes and involved in vesicular transport to the plasma membrane. By contrast, the less abundant PI(3,5)P<sub>2</sub> participates in endosomal vesicle trafficking. A reduced amount of PI(3,5)P<sub>2</sub> in cells leads to neuronal symptoms in the CNS and PNS [81]. Intriguingly, mutations in Fig 4, encoding a polyphosphoinositide phosphatase involved in synthesis and turnover of PI(3,5)P<sub>2</sub>, result in CMT type 4J [82]. Furthermore, mutations in *MTMR2*, encoding a phosphatase dephosphorylating PI3P and PI(3,5)P<sub>2</sub>, result in CMT type 4B1 [83]. These findings indicate that CMT subtypes linked to *NDRG1*, Fig 4 and *MTMR2* mutations may have a common defect in endosome-to-lysosome trafficking, as has been suggested earlier [84]. In fact, NDRG1 containing the CMT4D founding mutation R148X is unstable and unable to facilitate endosomal recycling [60].

The NDRG1 homolog in the sun flower (SF21) shows similarity to the ligand binding region of vertebrate inositol 1,4,5-triphosphate receptor (IP<sub>3</sub>R), and the same region is present in human (residues 179–279) and murine NDRG1 (Fig. 2) [29]. IP<sub>3</sub>R is an intracellular channel

that mediates  $\text{Ca}^{2+}$  release from the endoplasmic reticulum upon  $\text{IP}_3$  binding and therefore controls various  $\text{Ca}^{2+}$ -dependent cellular processes including fertilisation, cell proliferation, gene expression and apoptosis [85].  $\text{IP}_3$ -mediated  $\text{Ca}^{2+}$  signalling plays a role in Schwann cell proliferation and peripheral nerve myelination [86]. Furthermore, in human endothelial cells, NDRG1 interacts with phospholipase  $\text{C}\gamma 1$ , which mediates the production of  $\text{IP}_3$  and diacylglycerol from  $\text{PI}(4,5)\text{P}_2$ . The interaction happens through the phosphorylation sites in the NDRG1 C-terminal domain, but the requirement for NDRG1 phosphorylation is unknown [87].

$\text{PI}(4,5)\text{P}_2$  and  $\text{PI}(3,4,5)\text{P}_3$  are key players in the PI3K/AKT/mTOR signalling pathway, in which PI3K phosphorylates  $\text{PI}(4,5)\text{P}_2$  to  $\text{PI}(3,4,5)\text{P}_3$ , leading to AKT activation. NDRG1 has an inhibitory effect on AKT and the expression of mTOR [88] as well as on PI3K [70], and recently, NDRG1 was suggested to bind PI3K [89]. The direct binding to  $\text{PI}(4,5)\text{P}_2$  and  $\text{PI}(3,4,5)\text{P}_3$  could facilitate NDRG1 function in this pathway. In addition PTEN, a tumour suppressor, which antagonises the PI3K/AKT pathway by dephosphorylating  $\text{PI}(3,4,5)\text{P}_3$  [90], upregulates expression of *NDRG1* in prostate and breast cancer cells through an AKT-dependent pathway [36]. On the other hand, *PTEN* downregulation is correlated with NDRG1 upregulation in endometrial carcinoma [91]. However, NDRG1 upregulates PTEN in pancreatic cancer cells, possibly by increasing the stability or reducing proteasomal degradation [70], suggesting a positive feedback loop between NDRG1 and PTEN. Furthermore, SGK3, which binds PI3P to be directed to endosomes downstream of the PI3K pathway [92], mediates degradation of NDRG1 in breast cancer cells [93]. The PI3K/AKT/mTOR pathway has an important role in ErbB receptor signalling in peripheral myelination as well as in cancer metastasis [84,94]; NDRG1 has a fundamental role in these processes, and defects may lead to pathological consequences.

The C-terminal region of NDRG1 is phosphorylated in cells, which affects NDRG1 subcellular localisation [95]. Nevertheless, the phosphorylation of NDRG1 did not affect myelination in mice [20]. We did not study the phosphorylated forms of NDRG1<sub>fl</sub>, and it remains to be explored how phosphorylation affects the conformation of the C-terminal region or the molecular interactions of NDRG1.

### Disease variants

NDRG1 is expressed in myelin-forming cells, and it participates in myelin formation and maintenance [30,62,96]. Defects in *NDRG1* lead to a peripheral neuropathy, CMT4D. Several human CMT4D-associated

*NDRG1* mutations have been reported [4–7], and many of them lead to a premature termination of protein translation and truncated protein. However, two missense mutations, L146P and R234Q, were recently discovered [8]. Both Leu146 and Arg234 are conserved in all human NDRGs, as well as in all NDRG1 sequences of different species (Figs 1 and 2).

In the NDRG1 structure, Leu146 is located in the middle of the  $\alpha 5$  helix, its sidechain pointing towards the central  $\beta$  sheet in the core of the  $\alpha/\beta$  hydrolase fold (Fig. 8C). The L146P mutation is expected to induce a kink and disrupt the  $\alpha 5$  helix, affecting the hydrophobic core of the  $\alpha/\beta$  hydrolase domain, leading to unstable protein and the faster degradation of NDRG1 reported previously [8].

Arg234 points towards the canonical catalytic site and Asp64 and His194 in the crystal structure. Between these residues and Arg234, there is Tyr231 which forms a  $\pi$ - $\pi$  stacking interaction with Arg234 (Fig. 8D). The R234Q mutation leads to the loss of this interaction, altering local electrostatics, and it could affect the function of the putative catalytic site as well as protein stability.

The NDRG1 sequences are highly conserved within all mammals, including dogs (Fig. 2). The G98V mutation discovered in the Alaskan Malamute causes an inherited polyneuropathy with CMT-like symptoms [21]. Gly98 is conserved in all species, including plants. In the crystal structure of human NDRG1, this residue is embedded inside the  $\alpha/\beta$  hydrolase fold and induces a sharp turn in the main chain. As a small amino acid lacking the sidechain, Gly can form sharp turns in polypeptide chains and take conformations not accessible to other amino acids. A mutation in Gly98 may prevent adopting the correct main chain conformation and affect overall folding and protein stability. These observations suggest that Gly98 is a structurally central residue in the NDRG family.

### Concluding remarks

In conclusion, structural analyses reveal a highly dynamic nature of NDRG1, and conformational changes may take place in both the N- and C-terminal regions upon interaction with a ligand, such as a metal ion or lipid membrane (Fig. 8E). The crystal structure of the  $\alpha/\beta$  hydrolase domain provides novel information about the canonical  $\alpha/\beta$  hydrolase active site and residues potentially involved in metal binding in NDRG1. The structure sheds light on the likely effects of CMT-linked *NDRG1* mutations and the relationship of NDRG1 to other members of the NDRG subfamily of  $\alpha/\beta$  hydrolases. Further studies will be required to



elucidate the activities of the putative functional sites and their relevance to the cellular functions of NDRG1 as well as the molecular mechanisms of NDRG1-linked disease.

## Materials and methods

NDRG sequences were aligned with T-Coffee [97] and visualised using ESPript [98]. UniProtKB accession numbers were as follows: NDRG1 (Q92597-1), NDRG2b (Q9UN36-2), NDRG3 (Q9UGV2-1), NDRG4 (Q9ULP0-1), dog NDRG1 (L7V3M2-1), mouse NDRG1 (Q62433-1), zebrafish NDRG1 (Q6A3P5-1), fruit fly BcDNA : GH02439 (Q9Y164-1) and sunflower pollen-specific protein SF21 (Q23969-1).

## Cloning, protein expression and purification

A synthetic gene encoding full-length human NDRG1 (amino acids 1–394; UniProtKB: Q92597) was purchased from GenScript (Piscataway, NJ, USA). The cDNA was cloned into the pET28a(+)-tobacco etch virus (TEV) vector to produce a recombinant protein containing an N-terminal hexahistidine tag. The expression and purification procedures were identical for the full-length and truncated NDRG1 variants. The recombinant plasmid was transformed into *Escherichia coli* Rosetta (DE3) competent cells. The cells were cultured in autoinducing ZYM-5052 medium [99] supplemented with  $50 \mu\text{g}\cdot\text{mL}^{-1}$  kanamycin and  $34 \mu\text{g}\cdot\text{mL}^{-1}$  chloramphenicol for 4 h at 310.15 K and for 16 h at 293.15 K. The cells were collected by centrifugation at 5020 *g* for 40 min at 277.15 K. The cell pellets were resuspended in ice-cold buffer A (50 mM HEPES, pH 7.0, 500 mM NaCl, 10 mM imidazole pH 7.0 and 0.25 mM TCEP pH 7.0), and half a tablet of SigmaFAST™ Protease Inhibitor Cocktail Tablet, EDTA Free (Merck KGaA, Darmstadt, Germany) was added to the cell suspension prior to ultrasonication. The lysate was centrifuged at 30 600 *g* for 40 min at 4 °C. The supernatant was loaded onto HisPur™ Ni-NTA Resin (Thermo Fisher Scientific Inc., Waltham, MA, USA) pre-equilibrated with buffer A and incubated with the resin for 2 h at 4 °C. The resin was loaded to a column, the matrix was washed with buffer A containing 50 mM imidazole, and the resin-bound proteins were eluted with buffer A containing 500 mM imidazole. The protein was desalted with buffer B (20 mM HEPES pH 7.0, 200 mM NaCl and 0.25 mM TCEP pH 7.0) using a PD-10 Desalting Column with Sephadex G-25 Resin (GE Healthcare, Chicago, IL, USA). The hexahistidine tag was cleaved by incubation with His-tagged TEV protease at 303.15 K for 2 h, followed by Ni-NTA column chromatography using buffer B containing 50 mM imidazole. The eluted proteins were filtered using an Ultrafree-CL Centrifugal Filter (0.22  $\mu\text{m}$ , Merck KGaA) and loaded onto a

HiLoad 16/60 Superdex 75 column (GE Healthcare) equilibrated with buffer B. The purified protein was concentrated using a Vivaspin® Turbo 4 Ultrafiltration Unit (Sartorius, Göttingen, Germany) for further studies.

## Mutagenesis of truncated NDRG1 proteins

A vector containing C-terminally truncated NDRG1 (amino acids 1–319, NDRG1<sub>1–319</sub>) was produced from the NDRG1<sub>n</sub>-pET28aTEV plasmid by PCR using Phusion High-Fidelity DNA Polymerase (Thermo Fisher Scientific Inc.). The PCR products were digested with *DpnI*, purified using NucleoSpin Gel and PCR Clean-up kit (Macherey-Nagel, Düren, Germany) and transformed to Top10 cells. The recombinant vector was produced and isolated as for the full-length NDRG1 described above.

A vector containing the N-terminally truncated NDRG1 (NDRG1<sub>28–319</sub>, NDRG1<sub>31–319</sub> or NDRG1<sub>31–394</sub>) was produced by PCR from the plasmid containing the NDRG1<sub>1–319</sub> or NDRG1<sub>n</sub>, respectively, the PCR products were digested with *DpnI*, and DNA was extracted from a 0.8% agarose gel using the NucleoSpin Gel and PCR Clean-up kit (Macherey-Nagel). Plasmid DNA was ligated with T4 DNA ligase and transformed to Top10 cells. Colonies were screened by PCR using Taq polymerase and cultured in LB medium supplemented with  $50 \mu\text{g}\cdot\text{mL}^{-1}$  kanamycin, and the recombinant vector was isolated as for the full-length NDRG1 described above.

## Multiangle light scattering

SEC-MALS was used to determine the monodispersity and molecular weight of NDRG1 in solution. Chromatography was performed using a Shimadzu HPLC Unit and a Superdex 75 Increase 10/300 (GE Healthcare) column with 20 mM HEPES (pH 7.0), 200 mM NaCl, 0.25 mM TCEP (pH 7.5) as mobile phase. One hundred-microgram samples were injected into the column at an isocratic flow of  $0.5 \text{ mL}\cdot\text{min}^{-1}$ , and light scattering was recorded using a Wyatt miniDAWN TREOS instrument (Wyatt Technology, Santa Barbara, CA, USA). Protein concentration was determined using a Shimadzu refractometer. Data were analysed using the ASTRA software (Wyatt Technology).

## Crystallisation

NDRG1<sub>31–319</sub> was concentrated to  $17.2 \text{ mg}\cdot\text{mL}^{-1}$ , and initial crystallisation was performed with commercial screening kits (Molecular Dimensions, Maumee, OH, USA) using the sitting drop vapour-diffusion method at 20 °C. First crystals were produced using 1.4 M sodium malonate (pH 6.0). The crystals were further optimised with a screen containing 1.3–1.6 M sodium malonate (pH 5.75–6.50) and 5–15 mM TCEP (pH 7.0). The best crystals were grown at 285.15 K in drops

containing 200–300 nL of 16.6 mg·mL<sup>-1</sup> protein and 300–400 nL of crystallisation solution containing 1.4 M sodium malonate (pH 6.25), 10 mM TCEP (pH 7.0). Crystals were cryoprotected with 1.8 M sodium malonate (pH 6.25) and flash-frozen in liquid nitrogen prior to data collection.

### Data collection, refinement and structural determination

X-ray diffraction data were collected at the PETRA III (DESY, Hamburg, Germany) synchrotron, on beamline P11 [100] at 100 K. The X-ray diffraction data were processed and scaled using XDS [101]. The crystals belonged to the space group P4<sub>3</sub>2<sub>1</sub>2 with two molecules in the asymmetric unit. The structure was solved using molecular replacement with the structure of human NDRG2 (PDB ID: 2XMQ) [26] as a search model using Phaser-MR [102] in the PHENIX software [103]. The model was completed by iterative cycles of refinement using phenix.refine [104] and WinCoot [105]. The coordinates and structure factors were deposited to the PDB (PDB ID: 6ZMM).

### Small-angle X-ray scattering

SEC-SAXS data were collected from samples at 5–14 mg·mL<sup>-1</sup> at the Diamond Light Source (Didcot, UK) on beamline B21 and at SOLEIL (Saint Aubin, Essonne, France) on beamline SWING. SEC was performed using a Superdex 200 (GE Healthcare) or a BioSEC3-300 (Agilent Technologies, Santa Clara, CA, USA) column with buffer containing 20–50 mM HEPES (pH 7.0), 100–200 mM NaCl, 0.25 mM TCEP (pH 7.0). Data were processed and analysed using Foxtrot (SOLEIL) and ScÅtter (<http://www.bioisis.net/tutorials/9>), and model building was done with GASBOR [106] and EOM [68] from the ATSAS package [107].

### Lipid vesicle preparation

Phosphatidylinositol phosphates were purchased from Echelon Biosciences (Salt Lake City, UT, USA). POPC, DMPC and DMPG were purchased from Avanti Polar Lipids (Alabaster, AL, USA) and Anatrace (Maumee, OH, USA). Lipid stocks were prepared by dissolving dry lipids in chloroform : methanol : water (20 : 13 : 3 v/v). All mixtures were prepared from stocks at the desired molar ratios and dried under a stream of air. The dried lipids were resuspended in water, and the suspensions were clarified using Branson 450 Digital Sonifier (Marshall Scientific LLC, Hampton, NH, USA).

### Circular dichroism spectroscopy

CD spectra were measured from 1.0 μM protein samples in 10 mM HEPES (pH 7.0), 100 mM NaF, 0.10 mM TCEP

(pH 7.5), using quartz cuvettes with a 1.0-mm pathlength and a Chirascan CD Spectrometer (Applied Photophysics Ltd, Leatherhead, Surrey, UK). 100 μM of lipid vesicles or 5–50 μM of metallic salts was mixed with the protein prior to the measurement. Spectra were recorded twice for each sample from 198 to 280 nm at 25 °C. Buffer spectra were subtracted, and the sample spectra were averaged.

Synchrotron radiation circular dichroism data were collected from 0.5 mg·mL<sup>-1</sup> protein samples in 20 mM HEPES (pH 7.0), 150 mM NaF, 0.25 mM TCEP (pH 7.0) on the AU-CD beamline at the ASTRID2 synchrotron (ISA, Aarhus, Denmark). 1.43 mM lipid vesicles were mixed with the protein (P/L ratio 1 : 100) prior to measurement. Hellma® cylindrical absorption cuvette (Suprasil® quartz, Hellma GmbH & Co. KG, Müllheim, Germany) with a pathlength of 100 μm was used for the measurements. Spectra were recorded three times for each sample from 170 to 280 nm at 25 °C. Buffer spectra were subtracted, and the sample spectra were processed and averaged using CDtoolX [108]. Secondary structure deconvolutions were done with K2D3 [109].

### Lipid cosedimentation assay

One millimolar of lipid vesicles was mixed with 10 μM protein in 20 mM HEPES (pH 7.0) and 150 mM NaCl, and samples of 50 μL were incubated for 1 h at room temperature. Vesicles and bound proteins were sedimented by 1 h of ultracentrifugation at 434 500 *g* at 288.15 K using an Optima TL ultracentrifuge and a TLA-100 rotor (Beckman Coulter, Indianapolis, IN, USA). The pellets were resuspended, and both the soluble and sedimented fractions were analysed on SDS-PAGE. Fifty micromolar NiSO<sub>4</sub> was mixed with 10 μM protein and 1 mM POPC to see whether nickel affects POPC binding. The lipid cosedimentation assays were performed three times with each vesicle composition and protein construct. Gel bands were quantified using IMAGEJ [110].

### Protein stability analysis

Nano-DSF was used to study the stability of the different protein constructs and the effect of metals on the stability of NDRG1. Nano-DSF data were collected from 5 μM protein samples with 50 μM metallic salts in 20 mM HEPES (pH 7.0) and 150 mM NaCl using Prometheus NT.48 (NanoTemper Technologies GmbH, München, Germany).

### Isothermal titration calorimetry

The proteins were dialysed into 20 mM HEPES (pH 7.0), 100 mM NaCl, 0.10 mM TCEP (pH 7.5) and diluted to 30 μM. In total, 38.65 μL of 360 μM NiSO<sub>4</sub> was titrated into 280 μL of protein using a MicroCal iTC 200

calorimeter (GE Healthcare). All samples were prepared and measured twice. Data were analysed with ORIGIN (OriginLab Corporation, Northampton, MA, USA).

## Acknowledgements

This work was funded by Jane and Aatos Erkko Foundation and the Academy of Finland, grant number 315272. The research leading to this result has been supported by the project iNEXT, grant number 653706 and CALIPSOplus, grant number 730872, from the EU Framework Programme for Research and Innovation HORIZON 2020. We acknowledge DESY (Hamburg, Germany), a member of the Helmholtz Association HGF, for the provision of experimental facilities. Parts of this research were carried out at PETRA III, and we would like to thank P11 beamline personnel. We acknowledge the instrumentation and personnel at Diamond Light Source, instrument B21, at SOLEIL beamline SWING and at ISA, AU-CD. The use of the facilities and expertise of the Biocenter Oulu Proteomics and protein analysis and Structural Biology core facilities, members of Biocenter Finland, Instruct-ERIC Centre Finland and FIN-Struct, is gratefully acknowledged.

## Conflict of interest

The authors declare no conflict of interest.

## Author contributions

VM, PK and SR planned experiments; VM, GM, PK and SR performed experiments; VM, GM, PK and SR analysed data; PK, RL and SR contributed reagents or other essential material; VM, GM, PK and SR wrote the paper.

## Peer Review

The peer review history for this article is available at <https://publons.com/publon/10.1111/febs.15660>.

## References

- Norton WT & Poduslo SE (1973) Myelination in rat brain: changes in myelin composition during brain maturation. *J Neurochem* **21**, 759–773.
- Saporta MA & Shy ME (2013) Inherited peripheral neuropathies. *Neurol Clin* **31**, 597–619.
- Laurá M, Pipis M, Rossor AM & Reilly MM (2019) Charcot–Marie–Tooth disease and related disorders: an evolving landscape. *Curr Opin Neurol* **32**, 641–650.
- Kalaydjieva L, Hallmayer J, Chandler D, Savov A, Nikolova A, Angelicheva D, King RH, Ishpekova B, Honeyman K, Calafell F *et al.* (1996) Gene mapping in Gypsies identifies a novel demyelinating neuropathy on chromosome 8q24. *Nat Genet* **14**, 214–217.
- Okamoto Y, Goksungur MT, Pehlivan D, Beck CR, Gonzaga-Jauregui C, Muzny DM, Atik MM, Carvalho CMB, Matur Z, Bayraktar S *et al.* (2014) Exonic duplication CNV of NDRG1 associated with autosomal-recessive HMSN-Lom/CMT4D. *Genet Med* **16**, 386–394.
- Piscosquito G, Magri S, Saveri P, Milani M, Ciano C, Farina L, Taroni F & Pareyson D (2017) A novel NDRG1 mutation in a non-Romani patient with CMT4D/HMSN-Lom. *J Peripher Nerv Syst* **22**, 47–50.
- Chen B, Chen N, Niu S, Pan H, Wang X & Zhang Z (2018) A novel homozygous NDRG1 mutation in a Chinese patient with Charcot-Marie-Tooth disease 4D. *J Clin Neurosci* **53**, 231–234.
- Li L-X, Liu G-L, Liu Z-J, Lu C & Wu Z-Y (2017) Identification and functional characterization of two missense mutations in NDRG1 associated with Charcot-Marie-Tooth disease type 4D. *Hum Mutat* **38**, 1569–1578.
- Butinar D, Zidar J, Leonardis L, Popovic M, Kalaydjieva L, Angelicheva D, Sininger Y, Keats B & Starr A (1999) Hereditary auditory, vestibular, motor, and sensory neuropathy in a Slovenian Roma (Gypsy) kindred. *Ann Neurol* **46**, 36–44.
- Baethmann M, Göhlich-Ratmann G, Schröder JM, Kalaydjieva L & Voit T (1998) HMSNL in a 13-year-old Bulgarian girl. *Neuromuscul Disord* **8**, 90–94.
- Kalaydjieva L, Nikolova A, Turnev I, Petrova J, Hristova A, Ishpekova B, Petkova I, Shmarov A, Stancheva S, Middleton L *et al.* (1998) Hereditary motor and sensory neuropathy–Lom, a novel demyelinating neuropathy associated with deafness in gypsies. Clinical, electrophysiological and nerve biopsy findings. *Brain J Neurol* **121**, 399–408.
- King RHM, Tournev I, Colomer J, Merlini L, Kalaydjieva L & Thomas PK (1999) Ultrastructural changes in peripheral nerve in hereditary motor and sensory neuropathy-Lom. *Neuropathol Appl Neurobiol* **25**, 306–312.
- Kalaydjieva L, Gresham D, Gooding R, Heather L, Baas F, de Jonge R, Blechschmidt K, Angelicheva D, Chandler D, Worsley P *et al.* (2000) N-myc downstream-regulated gene 1 is mutated in hereditary motor and sensory neuropathy–Lom. *Am J Hum Genet* **67**, 47–58.
- Echaniz-Laguna A, Degos B, Bonnet C, Latour P, Hamadouche T, Lévy N & Leheup B (2007) NDRG1-linked Charcot-Marie-Tooth disease (CMT4D) with central nervous system involvement. *Neuromuscul Disord* **17**, 163–168.

- 15 Bruun CS, Jäderlund KH, Berendt M, Jensen KB, Spodsberg EH, Gredal H, Shelton GD, Mickelson JR, Minor KM, Lohi H *et al.* (2013) A Gly98Val mutation in the N-Myc downstream regulated gene 1 (NDRG1) in Alaskan Malamutes with polyneuropathy. *PLoS One* **8**, e54547.
- 16 Drögemüller C, Becker D, Kessler B, Kemter E, Tetens J, Jurina K, Jäderlund KH, Flagstad A, Perloski M, Lindblad-Toh K *et al.* (2010) A deletion in the N-Myc downstream regulated gene 1 (NDRG1) gene in Greyhounds with polyneuropathy. *PLoS One* **5**, e11258.
- 17 Okuda T, Higashi Y, Kokame K, Tanaka C, Kondoh H & Miyata T (2004) NdrG1-deficient mice exhibit a progressive demyelinating disorder of peripheral nerves. *Mol Cell Biol* **24**, 3949–3956.
- 18 Lachat P, Shaw P, Gebhard S, van Belzen N, Chaubert P & Bosman FT (2002) Expression of NDRG1, a differentiation-related gene, in human tissues. *Histochem Cell Biol* **118**, 399–408.
- 19 Berger P, Sirkowski EE, Scherer SS & Suter U (2004) Expression analysis of the N-Myc downstream-regulated gene 1 indicates that myelinating Schwann cells are the primary disease target in hereditary motor and sensory neuropathy-Lom. *Neurobiol Dis* **17**, 290–299.
- 20 Heller BA, Ghidinelli M, Voelkl J, Einheber S, Smith R, Grund E, Morahan G, Chandler D, Kalaydjieva L, Giancotti F *et al.* (2014) Functionally distinct PI 3-kinase pathways regulate myelination in the peripheral nervous system. *J Cell Biol* **204**, 1219–1236.
- 21 Skedsmo FS, Tranulis MA, Espenes A, Prydz K, Matiaszek K, Gunnes G, Hermansen LC & Jäderlund KH (2019) Cell and context-dependent sorting of neuropathy-associated protein NDRG1 - insights from canine tissues and primary Schwann cell cultures. *BMC Vet Res* **15**, 121.
- 22 Murray JT, Campbell DG, Morrice N, Auld GC, Shpiro N, Marquez R, Peggie M, Bain J, Bloomberg GB, Grahammer F *et al.* (2004) Exploitation of KESTREL to identify NDRG family members as physiological substrates for SGK1 and GSK3. *Biochem J* **384**, 477–488.
- 23 Kokame K, Kato H & Miyata T (1996) Homocysteine-respondent genes in vascular endothelial cells identified by differential display analysis: GRP78/BiP and novel genes. *J Biol Chem* **271**, 29659–29665.
- 24 Qu X, Zhai Y, Wei H, Zhang C, Xing G, Yu Y & He F (2002) Characterization and expression of three novel differentiation-related genes belong to the human NDRG gene family. *Mol Cell Biochem* **229**, 35–44.
- 25 Shaw E, McCue LA, Lawrence CE & Dordick JS (2002) Identification of a novel class in the alpha/beta hydrolase fold superfamily: the N-myc differentiation-related proteins. *Proteins Struct Funct Genet* **47**, 163–168.
- 26 Hwang J, Kim Y, Kang HB, Jaroszewski L, Deacon AM, Lee H, Choi W-C, Kim K-J, Kim C-H, Kang BS *et al.* (2011) Crystal structure of the human N-Myc downstream-regulated gene 2 protein provides insight into its role as a tumor suppressor. *J Biol Chem* **286**, 12450–12460.
- 27 Sevinsky CJ, Khan F, Kokabee L, Darehshouri A, Maddipati KR & Conklin DS (2018) NDRG1 regulates neutral lipid metabolism in breast cancer cells. *Breast Cancer Res* **20**, 55.
- 28 Kim KR, Kim KA, Park JS, Jang JY, Choi Y, Lee HH, Lee DC, Park KC, Yeom YI, Kim H-J *et al.* (2020) Structural and biophysical analyses of human N-Myc downstream-regulated Gene 3 (NDRG3) protein. *Biomolecules* **10**, 90.
- 29 Kräuter-Canham R, Bronner R, Evrard J-L, Hahne G, Friedt W & Steinmetz A (1997) A transmitting tissue- and pollen-expressed protein from sunflower with sequence similarity to the human RTP protein. *Plant Sci* **129**, 191–202.
- 30 Schonkeren SL, Massen M, van der Horst R, Koch A, Vaes N & Melotte V (2019) Nervous NDRGs: the N-myc downstream-regulated gene family in the central and peripheral nervous system. *Neurogenetics* **20**, 173–186.
- 31 Ghalayini MK, Dong Q, Richardson DR & Assinder SJ (2013) Proteolytic cleavage and truncation of NDRG1 in human prostate cancer cells, but not normal prostate epithelial cells. *Biosci Rep* **33**, 451–461.
- 32 Lee JE & Kim JH (2015) SUMO modification regulates the protein stability of NDRG1. *Biochem Biophys Res Commun* **459**, 161–165.
- 33 Shimono A, Okuda T & Kondoh H (1999) N-myc-dependent repression of Ndr1, a gene identified by direct subtraction of whole mouse embryo cDNAs between wild type and N-myc mutant. *Mech Dev* **83**, 39–52.
- 34 Li J & Kretzner L (2003) The growth-inhibitory NdrG1 gene is a Myc negative target in human neuroblastomas and other cell types with overexpressed N- or C-Myc. *Mol Cell Biochem* **250**, 91–105.
- 35 Kurdistani SK, Arizti P, Reimer CL, Sugrue MM, Aaronson SA & Lee SW (1998) Inhibition of tumor cell growth by RTP/rit42 and its responsiveness to p53 and DNA damage. *Cancer Res* **58**, 4439–4444.
- 36 Bandyopadhyay S, Pai SK, Hirota S, Hosobe S, Tsukada T, Miura K, Takano Y, Saito K, Commes T, Piquemal D *et al.* (2004) PTEN up-regulates the tumor metastasis suppressor gene Drg-1 in prostate and breast cancer. *Cancer Res* **64**, 7655–7660.

- 37 Lin TM & Chang C (1997) Cloning and characterization of TDD5, an androgen target gene that is differentially repressed by testosterone and dihydrotestosterone. *Proc Natl Acad Sci USA* **94**, 4988–4993.
- 38 Guan RJ, Ford HL, Fu Y, Li Y, Shaw LM & Pardee AB (2000) Drg-1 as a differentiation-related, putative metastatic suppressor gene in human colon cancer. *Cancer Res* **60**, 749–755.
- 39 Piquemal D, Joulia D, Balaguer P, Basset A, Marti J & Commes T (1999) Differential expression of the RTP/Drg1/Ndr1 gene product in proliferating and growth arrested cells. *Biochim Biophys Acta Mol Cell Res* **1450**, 364–373.
- 40 Zhang A-H, Rao JN, Zou T, Liu L, Marasa BS, Xiao L, Chen J, Turner DJ & Wang J-Y (2007) p53-dependent NDRG1 expression induces inhibition of intestinal epithelial cell proliferation but not apoptosis after polyamine depletion. *Am J Physiol-Cell Physiol* **293**, C379–C389.
- 41 Stein S, Thomas EK, Herzog B, Westfall MD, Rocheleau JV, Jackson RSI, Wang M & Liang P (2004) NDRG1 is necessary for p53-dependent apoptosis. *J Biol Chem* **279**, 48930–48940.
- 42 Kim K, Ongusaha PP, Hong Y-K, Kurdistani SK, Nakamura M, Lu KP & Lee SW (2004) Function of Drg1/Rit42 in p53-dependent mitotic spindle checkpoint. *J Biol Chem* **279**, 38597–38602.
- 43 Croessmann S, Wong HY, Zabransky DJ, Chu D, Mendonca J, Sharma A, Mohseni M, Rosen DM, Scharpf RB, Cidado J *et al.* (2015) NDRG1 links p53 with proliferation-mediated centrosome homeostasis and genome stability. *Proc Natl Acad Sci USA* **112**, 11583–11588.
- 44 Kovacevic Z & Richardson DR (2006) The metastasis suppressor, NdrG-1: a new ally in the fight against cancer. *Carcinogenesis* **27**, 2355–2366.
- 45 Motwani M, Sirotnak FM, She Y, Commes T & Schwartz GK (2002) Drg1, a novel target for modulating sensitivity to CPT-11 in colon cancer cells. *Cancer Res* **62**, 3950–3955.
- 46 Shah MA, Kemeny N, Hummer A, Drobnjak M, Motwani M, Cordon-Cardo C, Gonen M & Schwartz GK (2005) Drg1 expression in 131 colorectal liver metastases: correlation with clinical variables and patient outcomes. *Clin Cancer Res* **11**, 3296–3302.
- 47 Zhou D, Salnikow K & Costa M (1998) Cap43, a novel gene specifically induced by Ni<sup>2+</sup> compounds. *Cancer Res* **58**, 2182–2189.
- 48 Salnikow K, Blagosklonny MV, Ryan H, Johnson R & Costa M (2000) Carcinogenic nickel induces genes involved with hypoxic stress. *Cancer Res* **60**, 38–41.
- 49 Le NTV & Richardson DR (2004) Iron chelators with high antiproliferative activity up-regulate the expression of a growth inhibitory and metastasis suppressor gene: a link between iron metabolism and proliferation. *Blood* **104**, 2967–2975.
- 50 Park H, Adams MA, Lachat P, Bosman F, Pang SC & Graham CH (2000) Hypoxia induces the expression of a 43-kDa protein (PROXY-1) in normal and malignant cells. *Biochem Biophys Res Commun* **276**, 321–328.
- 51 Zhu H & Bunn HF (1999) Oxygen sensing and signaling: impact on the regulation of physiologically important genes. *Respir Physiol* **115**, 239–247.
- 52 Maxwell PH, Wiesener MS, Chang G-W, Clifford SC, Vaux EC, Cockman ME, Wykoff CC, Pugh CW, Maher ER & Ratcliffe PJ (1999) The tumour suppressor protein VHL targets hypoxia-inducible factors for oxygen-dependent proteolysis. *Nature* **399**, 271–275.
- 53 Zoroddu MA, Peana M, Medici S & Anedda R (2009) An NMR study on nickel binding sites in Cap43 protein fragments. *Dalton Trans* **28**, 5523–5534.
- 54 Zoroddu MA, Peana M, Kowalik-Jankowska T, Kozlowski H & Costa M (2004) Nickel(II) binding to Cap43 protein fragments. *J Inorg Biochem* **98**, 931–939.
- 55 Zoroddu MA, Kowalik-Jankowska T, Medici S, Peana M & Kozlowski H (2008) Copper(ii) binding to Cap43 protein fragments. *Dalton Trans*, 6127–6134.
- 56 Zoroddu MA, Medici S, Peana M & Anedda R (2010) NMR studies of zinc binding in a multi-histidinic peptide fragment. *Dalton Trans* **39**, 1282–1294.
- 57 Peana M, Medici S, Nurchi VM, Crisponi G, Lachowicz JI & Zoroddu MA (2013) Manganese and cobalt binding in a multi-histidinic fragment. *Dalton Trans* **42**, 16293.
- 58 Hunter M, Angelicheva D, Tournev I, Ingley E, Chan DC, Watts GF, Kremensky I & Kalaydjieva L (2005) NDRG1 interacts with APO A-I and A-II and is a functional candidate for the HDL-C QTL on 8q24. *Biochem Biophys Res Commun* **332**, 982–992.
- 59 Kachhap SK, Faith D, Qian DZ, Shabbeer S, Galloway NL, Pili R, Denmeade SR, DeMarzo AM & Carducci MA (2007) The N-Myc down regulated gene1 (NDRG1) is a Rab4a effector involved in vesicular recycling of E-cadherin. *PLoS One* **2**, e844.
- 60 Pietiäinen V, Vassilev B, Blom T, Wang W, Nelson J, Bittman R, Bäck N, Zelcer N & Ikonen E (2013) NDRG1 functions in LDL receptor trafficking by regulating endosomal recycling and degradation. *J Cell Sci* **126**, 3961–3971.
- 61 Askautrud HA, Gjernes E, Gunnes G, Sletten M, Ross DT, Børresen-Dale AL, Iversen N, Tranulis MA & Frengen E (2014) Global gene expression analysis reveals a link between NDRG1 and vesicle transport. *PLoS One* **9**, e87268.
- 62 King RHM, Chandler D, Lopaticki S, Huang D, Blake J, Muddle JR, Kilpatrick T, Nourallah M,

- Miyata T, Okuda T *et al.* (2011) NdrG1 in development and maintenance of the myelin sheath. *Neurobiol Dis* **42**, 368–380.
- 63 Schweitzer CJ, Zhang F, Boyer A, Valdez K, Cam M & Liang TJ (2018) N-Myc downstream-regulated gene 1 restricts hepatitis C virus propagation by regulating lipid droplet biogenesis and viral assembly. *J Virol* **92**, 1166.
- 64 Tu LC, Yan X, Hood L & Lin B (2007) Proteomics analysis of the interactome of N-myc downstream regulated gene 1 and its interactions with the androgen response program in prostate cancer cells. *Mol Cell Proteomics* **6**, 575–588.
- 65 Drozdetskiy A, Cole C, Procter J & Barton GJ (2015) JPred4: a protein secondary structure prediction server. *Nucleic Acids Res* **43**, W389–W394.
- 66 Mészáros B, Erdős G & Dosztányi Z (2018) IUPred2A: context-dependent prediction of protein disorder as a function of redox state and protein binding. *Nucleic Acids Res* **46**, W329–W337.
- 67 Krissinel E & Henrick K (2007) Inference of macromolecular assemblies from crystalline state. *J Mol Biol* **372**, 774–797.
- 68 Tria G, Mertens HDT, Kachala M & Svergun DI (2015) Advanced ensemble modelling of flexible macromolecules using X-ray solution scattering. *IUCr J* **2**, 207–217.
- 69 Salnikow K, Su W, Blagosklonny MV & Costa M (2000) Carcinogenic metals induce hypoxia-inducible factor-stimulated transcription by reactive oxygen species-independent mechanism. *Cancer Res* **60**, 3375–3378.
- 70 Kovacevic Z, Chikhani S, Lui GYL, Sivagurunathan S & Richardson DR (2013) The iron-regulated metastasis suppressor NDRG1 targets NEDD4L, PTEN, and SMAD4 and inhibits the PI3K and Ras signaling pathways. *Antioxid Redox Signal* **18**, 874–887.
- 71 Hayes RP, Green AR, Nissen MS, Lewis KM, Xun L & Kang C (2013) Structural characterization of 2,6-dichloro-p-hydroquinone 1,2-dioxygenase (PcpA) from *Sphingobium chlorophenolicum*, a new type of aromatic ring-cleavage enzyme. *Mol Microbiol* **88**, 523–536.
- 72 Garces F, Fernández FJ, Montellà C, Peña-Soler E, Prohens R, Aguilar J, Baldomà L, Coll M, Badia J & Vega MC (2010) Molecular architecture of the Mn<sup>2+</sup>-dependent lactonase UlaG reveals an RNase-like metallo- $\beta$ -lactamase fold and a novel quaternary structure. *J Mol Biol* **398**, 715–729.
- 73 Kasprzak K, Sunderman FW Jr & Salnikow K (2003) Nickel carcinogenesis. *Mutat Res Mol Mech Mutagen* **533**, 67–97.
- 74 Jomova K, Vondrakova D, Lawson M & Valko M (2010) Metals, oxidative stress and neurodegenerative disorders. *Mol Cell Biochem* **345**, 91–104.
- 75 Li Y, Jiao Q, Xu H, Du X, Shi L, Jia F & Jiang H (2017) Biometal dyshomeostasis and toxic metal accumulations in the development of Alzheimer's disease. *Front Mol Neurosci* **10**.
- 76 Weiler M, Blaes J, Pusch S, Sahm F, Czabanka M, Luger S, Bunse L, Solecki G, Eichwald V, Jugold M *et al.* (2014) mTOR target NDRG1 confers MGMT-dependent resistance to alkylating chemotherapy. *Proc Natl Acad Sci USA* **111**, 409–414.
- 77 Ji W, Yang L, Yu L, Yuan J, Hu D, Zhang W, Yang J, Pang Y, Li W, Lu J *et al.* (2008) Epigenetic silencing of O<sup>6</sup>-methylguanine DNA methyltransferase gene in NiS-transformed cells. *Carcinogenesis* **29**, 1267–1275.
- 78 Horne J, Jennings IG, Teh T, Gooley PR & Kobe B (2002) Structural characterization of the N-terminal autoregulatory sequence of phenylalanine hydroxylase. *Protein Sci* **11**, 2041–2047.
- 79 Khan FI, Lan D, Durrani R, Huan W, Zhao Z & Wang Y (2017) The lid domain in lipases: structural and functional determinant of enzymatic properties. *Front Bioeng Biotechnol* **5**.
- 80 Ruskamo S, Krokengen OC, Kowal J, Nieminen T, Lehtimäki M, Raasakka A, Dandey VP, Vattulainen I, Stahlberg H & Kursula P (2020) Cryo-EM, X-ray diffraction, and atomistic simulations reveal determinants for the formation of a supramolecular myelin-like proteolipid lattice. *J Biol Chem* **295**, 8692–8705.
- 81 Zhang Y, Zolov SN, Chow CY, Slutsky SG, Richardson SC, Piper RC, Yang B, Nau JJ, Westrick RJ, Morrison SJ *et al.* (2007) Loss of Vac14, a regulator of the signaling lipid phosphatidylinositol 3,5-bisphosphate, results in neurodegeneration in mice. *Proc Natl Acad Sci USA* **104**, 17518–17523.
- 82 Chow CY, Zhang Y, Dowling JJ, Jin N, Adamska M, Shiga K, Szigeti K, Shy ME, Li J, Zhang X *et al.* (2007) Mutation of FIG4 causes neurodegeneration in the pale tremor mouse and patients with CMT4J. *Nature* **448**, 68–72.
- 83 Bolino A, Muglia M, Conforti FL, LeGuern E, Salih MAM, Georgiou D-M, Christodoulou K, Hausmanowa-Petrusewicz I, Mandich P, Schenone A *et al.* (2000) Charcot-Marie-Tooth type 4B is caused by mutations in the gene encoding myotubularin-related protein-2. *Nat Genet* **25**, 17–19.
- 84 Lee S, Chin L-S & Li L (2017) Dysregulation of ErbB receptor trafficking and signaling in demyelinating Charcot-Marie-Tooth disease. *Mol Neurobiol* **54**, 87–100.
- 85 Mikoshiba K (2015) Role of IP3 receptor signaling in cell functions and diseases. *Adv Biol Regul* **57**, 217–227.
- 86 Heredia DJ, De Angeli C, Fedi C & Gould TW (2020) Calcium signaling in Schwann cells. *Neurosci Lett* **729**, 134959.

- 87 Watari K, Shibata T, Fujita H, Shinoda A, Murakami Y, Abe H, Kawahara A, Ito H, Akiba J, Yoshida S *et al.* (2020) NDRG1 activates VEGF-A-induced angiogenesis through PLC $\gamma$ 1/ERK signaling in mouse vascular endothelial cells. *Commun Biol* **3**, 107.
- 88 Dixon KM, Lui GYL, Kovacevic Z, Zhang D, Yao M, Chen Z, Dong Q, Assinder SJ & Richardson DR (2013) Dp44mT targets the AKT, TGF- $\beta$  and ERK pathways via the metastasis suppressor NDRG1 in normal prostate epithelial cells and prostate cancer cells. *Br J Cancer* **108**, 409–419.
- 89 Dai X, Fu Y & Ye Y (2020) Increased NDRG1 expression suppresses angiogenesis via PI3K/AKT pathway in human placental cells. *Pregnancy Hypertens* **21**, 106–110.
- 90 Maehama T & Dixon JE (1998) The tumor suppressor, PTEN/MMAC1, dephosphorylates the lipid second messenger, phosphatidylinositol 3,4,5-trisphosphate. *J Biol Chem* **273**, 13375–13378.
- 91 Chen J, Li S, Yang Z, Lu G & Hu H (2008) Correlation between NDRG1 and PTEN expression in endometrial carcinoma. *Cancer Sci* **99**, 706–710.
- 92 Tessier M & Woodgett JR (2006) Role of the Phox homology domain and phosphorylation in activation of Serum and glucocorticoid-regulated kinase-3. *J Biol Chem* **281**, 23978–23989.
- 93 Gasser JA, Inuzuka H, Lau AW, Wei W, Beroukhim R & Toker A (2014) SGK3 mediates INPP4B-dependent PI3K signaling in breast cancer. *Mol Cell* **56**, 595–607.
- 94 Sun J, Zhang D, Bae D-H, Sahni S, Jansson P, Zheng Y, Zhao Q, Yue F, Zheng M, Kovacevic Z *et al.* (2013) Metastasis suppressor, NDRG1, mediates its activity through signaling pathways and molecular motors. *Carcinogenesis* **34**, 1943–1954.
- 95 Park KC, Menezes SV, Kalinowski DS, Sahni S, Jansson PJ, Kovacevic Z & Richardson DR (2018) Identification of differential phosphorylation and sub-cellular localization of the metastasis suppressor, NDRG1. *Biochim Biophys Acta Mol Basis Dis* **1864**, 2644–2663.
- 96 Fang BA, Kovačević Ž, Park KC, Kalinowski DS, Jansson PJ, Lane DJR, Sahni S & Richardson DR (2014) Molecular functions of the iron-regulated metastasis suppressor, NDRG1, and its potential as a molecular target for cancer therapy. *Biochim Biophys Acta* **1845**, 1–19.
- 97 Notredame C, Higgins DG & Heringa J (2000) T-coffee: a novel method for fast and accurate multiple sequence alignment. *J Mol Biol* **302**, 205–217.
- 98 Robert X & Gouet P (2014) Deciphering key features in protein structures with the new ENDscript server. *Nucleic Acids Res* **42**, W320–W324.
- 99 Studier FW (2005) Protein production by auto-induction in high density shaking cultures. *Protein Expr Purif* **41**, 207–234.
- 100 Meents A, Reime B, Stuebe N, Fischer P, Warmer M, Goeries D, Roeber J, Meyer J, Fischer J, Burkhardt A *et al.* (2013) Development of an in-vacuum x-ray microscope with cryogenic sample cooling for beamline P11 at PETRA III. *Proceedings of SPIE* **8851**, 88510K.
- 101 Kabsch W (2010) XDS. *Acta Crystallogr D Biol Crystallogr* **66**, 125–132.
- 102 McCoy AJ, Grosse-Kunstleve RW, Adams PD, Winn MD, Storoni LC & Read RJ (2007) Phaser crystallographic software. *J Appl Crystallogr* **40**, 658–674.
- 103 Liebschner D, Afonine PV, Baker ML, Bunkoczi G, Chen VB, Croll T, Hintze B, Hung L-W, Jain S, McCoy A *et al.* (2019) Macromolecular structure determination using X-rays, neutrons and electrons: Recent developments in Phenix. *Acta Crystallogr Sect Struct Biol* **75**, 861–877.
- 104 Afonine PV, Grosse-Kunstleve RW, Echols N, Headd JJ, Moriarty NW, Mustyakimov M, Terwilliger TC, Urzhumtsev A, Zwart PH & Adams PD (2012) Towards automated crystallographic structure refinement with phenix.refine. *Acta Crystallogr D Biol Crystallogr* **68**, 352–367.
- 105 Emsley P, Lohkamp B, Scott WG & Cowtan K (2010) Features and development of Coot. *Acta Crystallogr Sect D* **66**, 486–501.
- 106 Svergun DI, Petoukhov MV & Koch MHJ (2001) Determination of domain structure of proteins from X-ray solution scattering. *Biophys J* **80**, 2946–2953.
- 107 Franke D, Petoukhov MV, Konarev PV, Panjkovich A, Tuukkanen A, Mertens HDT, Kikhney AG, Hajizadeh NR, Franklin JM, Jeffries CM *et al.* (2017) ATSAS 2.8: a comprehensive data analysis suite for small-angle scattering from macromolecular solutions. *J Appl Crystallogr* **50**, 1212–1225.
- 108 Miles AJ & Wallace BA (2018) CDtoolX, a downloadable software package for processing and analyses of circular dichroism spectroscopic data. *Protein Sci Publ Protein Soc* **27**, 1717–1722.
- 109 Louis-Jeune C, Andrade-Navarro MA & Perez-Iratxeta C (2012) Prediction of protein secondary structure from circular dichroism using theoretically derived spectra. *Proteins* **80**, 374–381.
- 110 Rueden CT, Schindelin J, Hiner MC, DeZonia BE, Walter AE, Arena ET & Eliceiri KW (2017) ImageJ2: ImageJ for the next generation of scientific image data. *BMC Bioinformatics* **18**, 529.